

CHALMERS

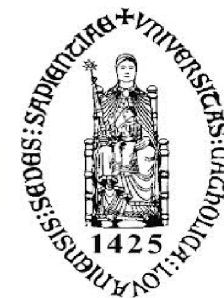


Engineered Tunnel Barriers for a $YBa_2Cu_3O_{7-\delta}$ Single Electron Transistor

Master's Thesis in Nanoscience and Nanotechnology

Zenas Van Veldhoven

Department of Microtechnology and Nanoscience
Quantum Device Physics
CHALMERS UNIVERSITY OF TECHNOLOGY
Göteborg, Sweden
Master's Thesis 2013-2014



Thesis for the Degree of Erasmus Mundus Master of Nanoscience and Nanotechnology

Engineered Tunnel Barriers for a $YBa_2Cu_3O_{7-\delta}$ Single Electron Transistor

Zenas Van Veldhoven

This thesis was carried out as a part of the Erasmus Mundus Master program in
Nanoscience and Nanotechnology with the trajectory Nanophysics.
KU Leuven- Chalmers University of Technology

Department of Microtechnology and Nanoscience
CHALMERS UNIVERSITY OF TECHNOLOGY
Göteborg, Sweden
Master's Thesis 2013-2014



Engineered Tunnel Barriers for a $YBa_2Cu_3O_{7-\delta}$ Single Electron Transistor

ZENAS VAN VELDHOVEN

© Zenas Van Veldhoven, 2014

Department of Microtechnology and Nanoscience
Chalmers University of Technology
SE 412 96 Gothenburg, Sweden
Telephone: +46 (0)31-772 10 00
Website: www.chalmers.se

Chalmers Reproservice
Gothenburg, Sweden 2014

Abstract

Despite the great scientific effort, the microscopic origin of superconductivity in the high-temperature superconductor $YBa_2Cu_3O_{7-\delta}$ is still not understood.

In recent work, Gustafsson, D. et al. discovered that the superconducting order parameter in a $YBa_2Cu_3O_{7-\delta}$ mesoscopic island did not have a purely d-wave symmetry, as it is commonly assumed. By using a Single-Electron Transistor (SET) made of a $YBa_2Cu_3O_{7-\delta}$ source, mesoscopic island, drain and gate, they discovered that the $YBa_2Cu_3O_{7-\delta}$ island had a fully gapped superconductivity. This indicates the existence of a subdominant imaginary order parameter in $YBa_2Cu_3O_{7-\delta}$ that gaps the nodes of the d-wave order parameter.

In order to investigate the doping dependence of this subdominant order parameter, one should use a new design for the SET, with normal metal source, drain and gate. To have a working SET, the tunnel resistance between the electrodes and the islands needs to be higher than the quantum resistance.

The goal of this work is to engineer the $YBa_2Cu_3O_{7-\delta}$ -Au tunnel junction with a sufficiently high tunnel resistance. For that, tunnel barriers between $YBa_2Cu_3O_{7-\delta}$ and Au were created by an Ar ion milling procedure of the surface using different etching times and different voltages. The current-voltage characteristics of the Au- $YBa_2Cu_3O_{7-\delta}$ junctions were investigated and the contact resistivity between $YBa_2Cu_3O_{7-\delta}$ and Au was measured.

The surface etching seems to create low transparency interfaces. In addition, a normal $YBa_2Cu_3O_{7-\delta}$ layer is formed at the surface, which can be turned superconducting by ozone treatment. Suitable tunnel barriers for a $YBa_2Cu_3O_{7-\delta}$ SET can be created using mild surface etching and ozonation.

Acknowledgements

I would like to thank my supervisor, Professor Floriana Lombardi, for given me the chance to work on this project and her guidance throughout the entire project. Thilo Bauch mini-lessons and explanations were invaluable to help me understand encountered problems and the complex field of high temperature superconductors.

I am very grateful to my daily supervisor, Reza Baghdadi, without whom this project would have been impossible. He has been an excellent teacher, both in and outside the cleanroom. In addition, his patience and the amount time he was willing to put into this project both speak to his character.

Thirdly, I would like to thank my co-promotor, Professor Victor Moshchalkov, for his willingness to evaluate this thesis and introducing me to the field of superconductivity. I would also like to thank the other Phd-students in my group, Marco, Sophie and Riccardo, for always be willing to help me out and offer such a nice working environment.

On a more personal note, I am grateful to my friends and family for their support and all the good times.

More specifically, I would like to say thanks to my old friends for never giving up on me and all the great stories. Thanks to my nano-friends for being such an awesome gang and all the shared curses and inside jokes this last two years. Thanks to my erasmus friends in Goteborg for the shared drinks, laughs and songs.

Thanks to my little brother, for letting me be a big brother, and my big sister, for having my back throughout the years.

I would like to thank are my mother, for letting me get away with chores if I was reading, and my father, for never giving the easy explanation, even if that entails explaining biochemistry to a 8-year old, and giving me that old microscope.

Zenas Van Veldhoven, Göteborg August 25, 2014

Contents

1	Introduction	1
2	Introduction to Superconductivity and the high-temperature superconductor $YBa_2Cu_3O_{7-\delta}$	4
2.1	A Brief Review of the Main Superconductors	4
2.2	Low-Temperature superconductors: materials, superconducting properties and theory	5
2.3	High-Temperature Superconductors: properties, materials and elusive theory	7
2.4	The High Temperature Superconductor $YBa_2Cu_3O_{7-\delta}$	8
2.4.1	The elusive theoretical explanation and sub-dominant order parameter	10
3	The Single Electron Transistor as a Spectroscopic Tool for Investigating the order parameter in $YBa_2Cu_3O_{7-\delta}$	12
3.1	Basic working mechanisms of a Single Electron Transistor	12
3.1.1	Principles of operation	12
3.2	Experimental Observation of sub-dominant order parameter in all $YBa_2Cu_3O_{7-\delta}$ SET	17
3.3	Follow-up Research	19
4	Engineering the Tunnel Barrier for a NISIN $YBa_2Cu_3O_{7-\delta}$ Single Electron Transistor	20
4.1	Motivation behind the thesis project	20
4.2	Methods to Engineering the interface $Au-YBa_2Cu_3O_{7-\delta}$	21
4.3	Outline of experimental work to investigate the Au(or Pt)- $YBa_2Cu_3O_{7-\delta}$ interface and the effect of mild ion etching	22
5	Tunneling characteristics of normal metal - insulator - superconductor junctions	23

5.1	Metallic and tunnelling characteristics of normal metal- LTS superconductor junctions	23
5.1.1	IV characteristics of a NIS junction	24
5.1.2	IV characteristics of a NS junction	24
5.1.3	Bridging the two regimes, the BTK approach	26
5.2	Metallic and tunnelling characteristics of normal metal- HTS superconductor junctions	28
5.3	The Effect of an Inhomogeneous Superconducting Electrode	31
6	Device Layout, Fabrication Process and Measurement Set-up	36
6.1	Introduction	36
6.2	Measuring the contact resistance: Concept and Device Layout	37
6.3	Fabrication process	40
6.4	Ozonation treatment	46
6.5	Evolution of the Device Layout and Fabrication Process	46
6.5.1	Evolution of Device Layout	46
6.5.2	Evolution of the fabrication process	48
6.6	Measurement set-up	49
7	Results and Discussion	51
7.1	Introduction	51
7.2	The critical current density of the $YBa_2Cu_3O_{7-\delta}$ nanowires	52
7.3	IV characteristics of the no treatment sample before and after ozonation	53
7.3.1	IVC before ozonation	53
7.3.2	IVC after Ozonation	54
7.3.3	The contact resistance before and after ozonation for no treatment sample	57
7.3.4	Interpretation of the results: the non treated interface and effect of ozonation	60
7.4	The IV characteristics of the 200V 5min sample	62
7.4.1	IVC before ozonation	62
7.4.2	IV and conductance curves after ozonation	63
7.4.3	Extracting the contact resistance	65
7.4.4	Interpretation of the results: the 200V 5min interface and effect of ozonation	65
7.5	The IV characteristics of the 250V for 5 minutes device	66
7.6	Follow-up Research	66
7.7	Conclusion	67
	Bibliography	71

1

Introduction

Superconductivity is a remarkable state of matter that exist at low temperatures in a variety of materials. It was first discovered in metals a hundred years ago, but in the 1980 other materials were shown to be superconducting. The most important among those new superconducting materials are the cuprates, like $YBa_2Cu_3O_{7-\delta}$, which are very different from metals, both in crystal structure as normal state and superconducting properties.

The microscopic origin of superconductivity is the pairing of electrons to form Cooper pairs, which condense into a single state that much resembles a Bose-Einstein condensate. Since the Cooper pairs in this condensate are phase coherent, they can be described by a single wave function, which is often referred to as the superconducting order parameter. Only for metals is the mechanism of this electron pairing completely understood and explained by the BCS theory. One of the main features of all superconductors is the presence of a gap in the density of states of quasiparticles at the Fermi energy level. The symmetry of the gap is related to the symmetry of the superconducting condensate and as such gives an indication of the underlying mechanism of superconductivity. For example, in metals the gap is isotropic, which reflects the electron-phonon coupling mechanism that causes the formation of Cooper pairs. The gap is also easily experimental accessible and is thus often used to learn more about superconductivity in different materials.

A theoretical explanation of the microscopic origin of superconductivity in $YBa_2Cu_3O_{7-\delta}$ has not yet been found, but a lot of the properties of the superconducting state are already known from experiments. Two of their main features are the dependence of the critical temperature on the oxygen doping of $YBa_2Cu_3O_{7-\delta}$ and the d-wave symmetry of the superconducting order parameter. One of the most recent discoveries was the existence of a complex subdominant order parameter in a $YBa_2Cu_3O_{7-\delta}$ island, in addition to the dominant d-wave order parameter. It was shown to exist using a single-electron transistor, with source, drain and island made out of $YBa_2Cu_3O_{7-\delta}$ and the

grain boundaries between them functioning as tunnel barriers.

Information about the doping dependence of the subdominant order parameter would be very interesting. Since it is difficult to maintain both the quality of the grain boundaries tunnel junction properties and control the doping of the island at the same time, a new single-electron transistor design is necessary. This requires to fabricate a new single-electron transistor with a noble metal source and drain electrode. To obtain a working single-electron transistor, the tunnel barriers between source/drain and island need to have a tunnel resistance higher than the quantum resistance. However, noble metals make very good contact with $YBa_2Cu_3O_{7-\delta}$, thus a tunnel barrier needs to be engineered.

This thesis focus on the engineering of the tunnel barrier between the noble metals Au and Pt and $YBa_2Cu_3O_{7-\delta}$ at the nanoscale, using mild ion etching of the $YBa_2Cu_3O_{7-\delta}$ surface.

Chapter 2 starts with an overview of the major discoveries in superconductivity to give some historical and general perspective. The origin of superconductivity in metals and their superconducting properties, including the gap and order parameter, are discussed as preparation of (and to contrast with) the superconducting properties of the cuprates. The structure and superconducting properties of $YBa_2Cu_3O_{7-\delta}$ are discussed in detail, with the main focus being on the symmetry of their order parameter and their doping dependence. To conclude, an allusion is made to the missing theoretical explanation of the microscopic origin of superconductivity and the existence of a complex subdominant order parameter as a "missing piece" of knowledge.

The next chapter gives a brief explanation of the basic working mechanisms of a single-electron transistor and how it can be used to probe the superconducting gap and gain information about the symmetry of the order parameter. Special attention is also paid to the two requirements for a working single electron transistor, namely that the charging energy of the island is larger than the thermal energy and the resistance of the tunnel barriers is higher than the quantum resistance. The previous experiment that first proved the existence of the subdominant order parameter using an all $YBa_2Cu_3O_{7-\delta}$ single electron transistor is then explained, as well as the follow-up research. As mentioned earlier, to investigate the doping dependence noble metal need to be used as source and drain material.

Chapter 4 starts with summarizing the motivation behind this thesis project in a more elaborated way and details why the change to a noble metal is necessarily. The different possible approaches to create a tunnel barrier are then discussed and our choice for mild ion etching is explained. The chapter ends with outlining the necessarily experimental work to engineer these tunnel barriers and why we want to investigate the effect of ozone treatment on the interface.

In chapter 5 a theoretical overview of the current-voltage characteristics of normal metal-superconductor and normal metal-insulator-superconductor is presented to help with the interpretation of our obtain experimental results in chapter 7.

Our approach to measure the contact resistance between Au- $YBa_2Cu_3O_{7-\delta}$ is explained in chapter 6. In addition, the fabricated device layout is discussed, as well as the fabrica-

tion process and measurement setup. There is also a section that details the difficulties that had to be overcome in the fabrication process and how the device layout changed from the initial samples, whose results had to be discarded.

The obtained results are presented and discussed in chapter 7. The current-voltage characteristics of the $\text{Au-YBa}_2\text{Cu}_3\text{O}_{7-\delta}$ interface are discussed for a sample that did not undergo any etching of the surface, and two samples whose surfaces were etched with 200V for 5 minutes and 250V for 5 minutes respectively. In addition, the effect of ozonation on the interface and critical current density is discussed.

In conclusion, it is shown that good tunnel barriers can be fabricated with sufficiently high tunnel resistance by mild ion etching the surface and ozone treatment.

2

Introduction to Superconductivity and the high-temperature superconductor $YBa_2Cu_3O_{7-\delta}$

2.1 A Brief Review of the Main Superconductors

Superconductivity is a remarkable phenomenon observed in certain materials at sufficiently low temperature. The two basic properties are zero resistance, $R = 0$, and perfect diamagnetism, $\vec{B} = 0$, inside the material. The superconducting state only exists below a specific temperature and magnetic field strength and it is destroyed for currents higher than a critical value. These three parameters are referred to as the critical temperature T_c , the critical field H_c , and the critical current density j_c and are all mutually dependent on each other.

The origin of superconductivity lies in the formation of phase coherent Cooper pairs. As a superconductor is cooled down below T_c , electrons with opposite spin near the Fermi level start to pair up to form Cooper pairs. These are boson-like particles with integer spin and they condense into a single state, much like bosons condense into a Bose-Einstein ground state at low temperatures. This superconducting condensate acts as a superfluid, it flows without resistance and carries no entropy.

Superconductivity was first discovered in 1911 by Kamerlingh Onnes when he observed a sudden drop to zero resistance in Hg upon cooling down to 4K [18]. Some other metals were also quickly discovered to be superconducting, including Al, Nb, Ti and Pb. Perfect diamagnetism was discovered in 1933 by Meisnner and the isotope effect in 1950[27], which indicated that phonons played a role in the formation of the superconducting state. A full theoretical understanding and description of the superconductivity in these metals

was only achieved in 1957, when Bardeen, Cooper and Schrieffer proposed the Bardeen-Cooper-Schrieffer (BCS) theory of superconductivity [4]. Previously, some important phenomenological theories were postulated, namely the two fluid model, the London theory and the Ginzburg-Landau theory. The next big discovery in the field of superconductivity was in the late seventies and eighties with the discovery of unconventional superconductors. While the superconductivity in simple metals could be explained by the BCS theory, these new superconductors were more complex. The first to be discovered were the heavy fermion superconductors in 1979 [35], quickly followed by organic superconductors in 1980 [5] and cuprates superconductors in 1986-87. The cuprates exhibit much higher critical temperature than previously known, up to 138K at ambient pressure for $HgBa_2Ca_2Cu_3O_x$ [33]. Due to the big differences in both superconducting properties and normal state properties between metals and the other superconductors, these two classes became known as conventional and unconventional superconductors, with the first class being fully explained by the BCS theory. Among the unconventional superconductors, the cuprates have received great attention due to their very high critical temperatures. The metallic superconductors are also referred to as Low Temperature Superconductors (LTS) and the cuprates as High Temperature Superconductors (HTS). It is important to note that despite almost 25 year of intense scientific research since the discovery of the cuprates, there is still no satisfactory theoretical explanation for the mechanism of high temperature superconductivity, or for the superconductivity of the other unconventional superconductors [29].

2.2 Low-Temperature superconductors: materials, superconducting properties and theory

Low temperature conventional superconductors are all metals or metal alloys. Their crystal structure is simple and their normal properties are all isotropic.

Niobium has the highest T_c of 9,25 K of all pure metals, while the alloys have critical temperatures up to 23,2 K.

Two important characteristic length scales in superconductors are the London penetration depth, λ_L , which gives the decay length of the magnetic field inside the superconductor, and the coherence length ξ , which reflects the size of a Cooper pair.

The superconducting state of low-temperature superconductors is theoretically explained by the BCS theory [4]. Cooper pairs are formed due to electron-phonon interaction. As an electron with energy near the Fermi energy, E_f with momentum $+p$ and spin \uparrow travels through the lattice of metal nuclei, it attracts the nuclei due to Coulomb interaction, causing them to move away from their equilibrium position. However, due to their much larger mass, this nuclear displacement lags behind on the movement of the electron. The result is a net local polarization of the lattice by one electron. This locally induced positive net charge of the lattice can then attract another electron with momentum $-p$ and spin \downarrow . If the attraction between two electrons due to the lattice polarization becomes greater than their coulombic repulsion, the electrons pair up to form Cooper pairs, which then condense into a superconducting condensate.

The superconducting condensate lies in the middle of a gap in the density of states at the Fermi level, while the states below and above the gap can be occupied by quasiparticle excitations of the superconducting state (similar to electrons and holes), in accordance with the Fermi distribution function. The gap energy is denoted as Δ , with 2Δ is the energy required to break a Cooper pair and create quasiparticle excitations. The gap energy is temperature dependent and goes to zero for $T = T_c$.

Since all Cooper pairs are phase coherent, they can be described by the same wavefunction $\Psi(\vec{r}, \phi) = \Psi_o(\vec{r})exp^{i\phi}$, with $|\Psi_o(r)|^2$ the density of the Cooper pairs and ϕ the phase of the superconducting condensate. This wavefunction is commonly referred to as the superconducting order parameter in the framework of the Ginzburg-Landau theory and describes the macroscopic phase-coherence of the pairs state. It can be shown that the amplitude $|\Psi_o(r)|^2$ corresponds to the pair amplitude of the cooper pairs in the BCS theory for T close to T_c , which in itself is proportional to the gap $\vec{\Delta}(\vec{r})$. As such, the symmetry of the gap gives information about the symmetry of the order parameter, or the macroscopic phase-coherent superconducting state.

It is important to note that the gap can be experimentally probed. Thus, information about the order parameter and superconducting condensate can be gained from spectroscopic studies of the gap.

The superconducting state is fully gapped in LTS. The Fermi surface is spherical and the superconducting gap exist over the entire surface of the sphere, thus the order parameter has a s-wave symmetry.

An illustration of the superconducting gap in metals is given in figure 2.1.

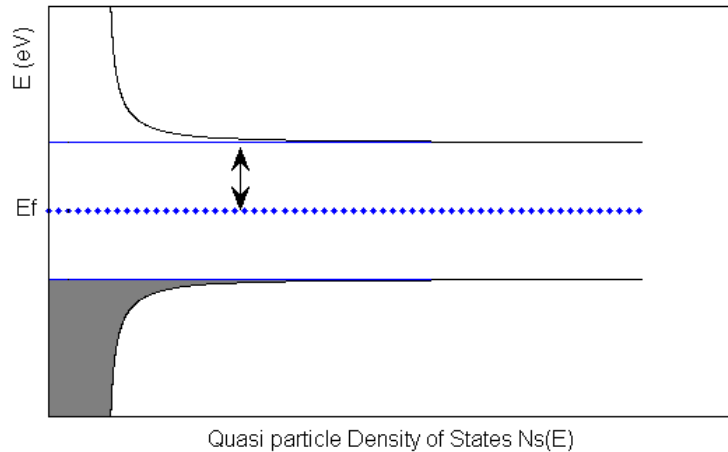


Figure 2.1: A schematic representation of the excitation density of excited states, N_s in a LTS superconductor at $T = 0$. The superconducting condensate lies at the Fermi level in the middle of the gap. The grey area indicates the filled states and the double arrow the size of the gap energy Δ .

2.3 High-Temperature Superconductors: properties, materials and elusive theory

The first HTS was discovered in 1986 [6]. It was a derivative of the ceramic perovskite LaCuO, that became superconducting upon doping with Ba, which replaces the La atoms in the crystal structure. The resulting superconductor is LaBaCuO₄ (LBCO) has a critical temperature of 35 K, higher than any known superconductor at that time. In addition, LBCO is a bad metal in the normal state. Both the high T_c as the superconductivity in a bad conducting material drew immediate scientific attention. Quickly, other perovskite ceramic materials were found to be superconductors with high critical temperatures.

The most intensely studied is $YBa_2Cu_3O_{7-\delta}$, which was discovered in 1987 with a T_c of 92 K [43]. In 1988 BSCCO and TBCCO were discovered, having a T_c of 107 K and 125 K respectively [26][34]. The highest T_c at ambient pressure is currently held by $HgBa_2Ca_2Cu_3O_x$ at 138 K [33].

All these HTS have a (defected) perovskite structure at the basis of their crystal structure. Perovskites typically consist of oxygen and two different cation, A and B, with following stoichiometry: ABO_3 . Their crystal structure is cubic, with the B cations sitting on the corners of the cubic unit cell, while the A cation occupies the center of the cube, and the oxygen atoms are placed at the middle of the edges [7]. In HTS, the B cation is always copper. The total unit cell consist of different perovskite unit cells stacked on top of each other, with sometimes other cations in between forming a two-dimensional layered material with copper oxide planes. These copper oxide planes are present in all HTS, including $YBa_2Cu_3O_{7-\delta}$, as can be seen in figure 2.2.

All cuprates have similar superconducting properties. The T_c is highly dependent on the level of hole or electron doping of the material [10]. Doping is achieved by replacing the A cation with another cation with more or less free electrons, like in LBCO, or by varying the oxygen content, like in $YBa_2Cu_3O_{7-\delta}$. In addition, HTS are bad metals at room temperature [44], have a d-wave order parameter [40] and a very complex phase diagram, with transition from insulating to antiferromagnetic to superconducting state, depending on the doping level [10].

A lot of effort has been made to understand the origin of superconductivity in the HTS. The BCS theory is not able to explain the high T_c and no clear isotope effect has been observed in the cuprates. These facts point towards a new mechanism of Cooper pair formation and phase coherence. Currently, there are various theories attempting to explain the superconductivity of the cuprates, but none seem to be satisfactory. This might indicate the existence of a "missing piece" of knowledge about the superconducting properties of the HTS [29].

2.4 The High Temperature Superconductor $YBa_2Cu_3O_{7-\delta}$

$YBa_2Cu_3O_{7-\delta}$ is one of the most extensively studied HTS, due to the ease of experimental access. It is often used as a model for the other superconducting cuprates, both experimentally as theoretically.

The crystal structure of $YBa_2Cu_3O_{7-\delta}$ consists of three defected perovskite unit cells stacked on top of each other, with a Yttrium cation in the middle cell and a Ba cation in the other two. A $YBa_2Cu_3O_{7-\delta}$ unit cell is shown in figure 2.2. The lattice parameters are $a \approx 3.88\text{\AA}$, $b \approx 3.82\text{\AA}$ and $c \approx 11.7\text{\AA}$ [12]. The perovskite cells consist of Cu as the B cation, that occupies the corners, Barium or Yttrium as the A cation in the center and Oxygen in the middle of the edges of the cube. There are strategic oxygen vacancies in the $YBa_2Cu_3O_{7-\delta}$ unit cell that dissolve the three-dimensionality of the oxygen lattice [32]. These oxygen vacancies create CuO chains in the b-axis direction and CuO_2 planes in the a-b plane located right above and under the Yttrium cation, while the CuO chains are on the other side of the Barium cation and run parallel to the CuO_2 planes.

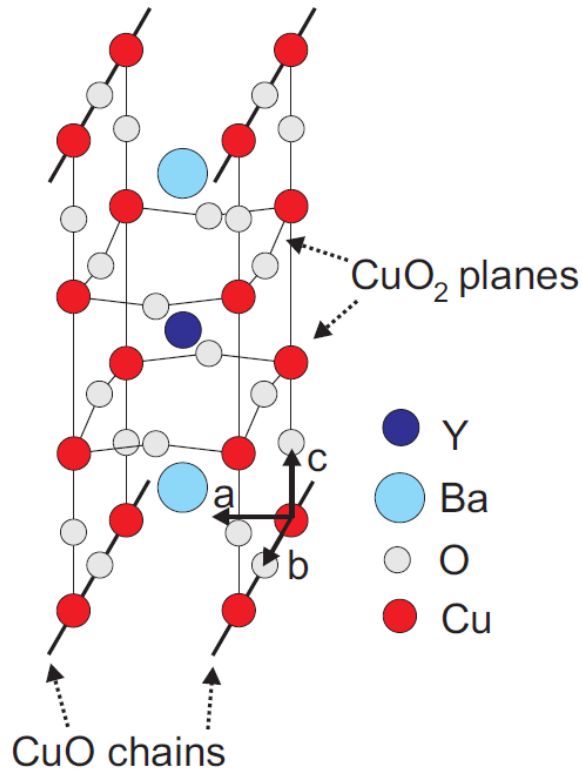


Figure 2.2: The unit cell of $YBa_2Cu_3O_{7-\delta}$. From [16]

$YBa_2Cu_3O_{7-\delta}$ and all other cuprates are characterized by high transition temperatures, which cannot be explained by the BCS theory. In addition, the cuprates have numerous properties which are remarkably different from the metal superconductors, which will be discussed below for the specific case of $YBa_2Cu_3O_{7-\delta}$, although most of them are common to all cuprates.

$YBa_2Cu_3O_{7-\delta}$ has different phases, depending on the oxygen content or hole doping of the material [10]. The δ in the chemical formula $YBa_2Cu_3O_{7-\delta}$ denotes the free doping of the material. phase diagram of $YBa_2Cu_3O_{7-\delta}$ can be seen in figure 2.3. Upon increasing the hole doping, it changes from the antiferromagnetic phase to the pseudogap phase. Here, there exist a gap in the electron density of states for reasons still debated [30], but this gap does not relate to the superconducting gap. Further increasing the doping level, $YBa_2Cu_3O_{7-\delta}$ makes a transition to a strange metal phase at high temperatures, or becomes superconducting for lower temperatures, as can be seen in figure 2.3. The superconducting dome is the region in the phase diagram where $YBa_2Cu_3O_{7-\delta}$ is superconducting. The critical temperature shows a bell-shape like dependence on the doping level. For higher doping levels and temperatures, $YBa_2Cu_3O_{7-\delta}$ forms a Fermi liquid phase. All these different phases makes $YBa_2Cu_3O_{7-\delta}$ a very complex material to study. Of special interest is the superconducting dome where the superconducting properties change with the doping level and the possible existence of a quantum critical points inside the dome [29]. Further insights into the doping dependence would greatly improve our understanding of the origin of superconductivity in the cuprates.

The superconducting properties of $YBa_2Cu_3O_{7-\delta}$ are also very anisotropic, the coherence length ξ in the a-b direction for optimally doped $YBa_2Cu_3O_{7-\delta}$ is 1-2 nm and 0.24 nm in the c direction, while the London penetration depth λ_L is 135 and 1000nm in the two directions [45][19]. This reflects the anisotropy of the 2D-layered crystal structure of the material, with the superconducting condensate existing in the 2D CuO_2 planes and a weak coupling between the planes in the c-direction.

In contrast to the isotropic s-wave symmetry of the order parameter in metal superconductors, the order parameter in HTS has a d-wave symmetry, $d_{x^2-y^2}$, as was shown by several phase sensitive experiments, for example by Tsuei et al. [40]. The shape of the HTS order parameter is illustrated in figure 2.4a). It consist of 4 lobes with a π -phase shift between each lobe. Between the lobes are nodes, where the superconducting gap vanishes. This means that the superconductivity in HTS is not fully gapped. As such, transport and tunnel properties of HTS are highly dependent on the orientation of the HTS.

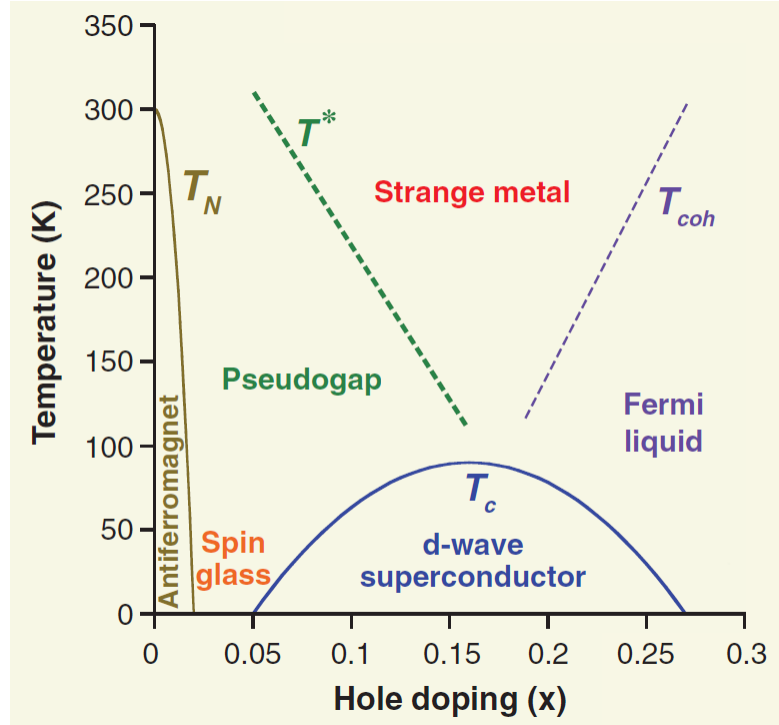


Figure 2.3: A schematic representation of the phase diagram of $YBa_2Cu_3O_{7-\delta}$ as a function of the hole doping x . The critical temperature of the superconducting phase has a dome-like dependence on the doping level. From [29]

2.4.1 The elusive theoretical explanation and sub-dominant order parameter

As mentioned already previously, no good theoretical explanation for the microscopic origin of superconductivity in cuprates has been found. The existence of a complex subdominant order parameter has been theoretically predicted. This imaginary order parameter would either have a *is*-wave symmetry, as predicted by [14], or a *id*-wave symmetry, as predicted by [25] and [3] and is illustrated in figure 2.4. Regardless of the symmetry, it would cause the nodal regions to become gapped, making $YBa_2Cu_3O_{7-\delta}$ a fully gapped superconductor. The existence of this subdominant order parameter, its symmetry and its properties would provide an important piece of information to confirm and improve the existing theories.

Experimental efforts were made to prove its existence from probing the Landau levels of quasiparticle states along the nodal direction [13], penetration depth measurements [21], observed plateaus in thermal conductivity [24] and the quantization of spontaneous generated flux in a HTS superconducting ring with one section made of a LTS [22]. However, the first conclusive evidence was found by Gustaffson et al. [17] in 2013, using a single-electron transistor to probe the superconducting gap.

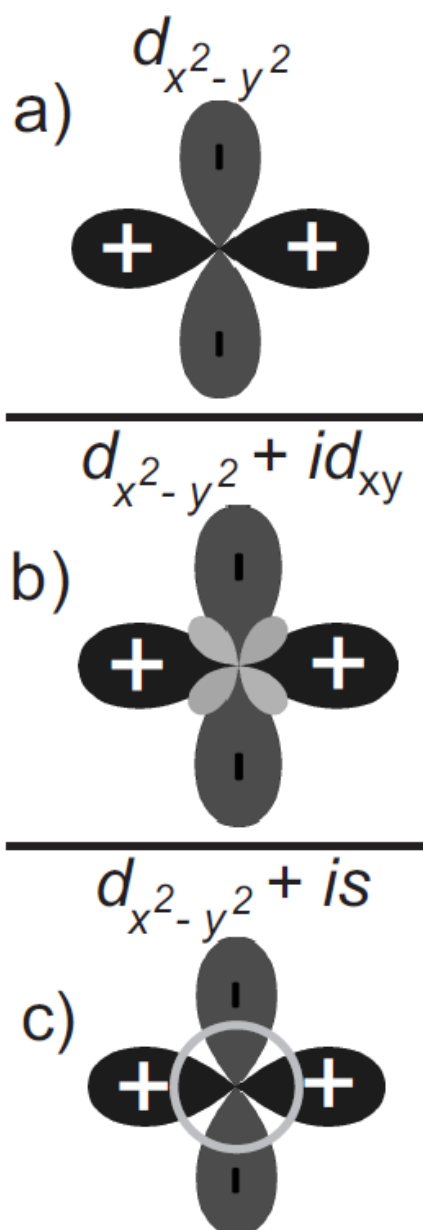


Figure 2.4: A schematic representation of the pure d-wave order parameter (a), with a complex id_{xy} component (b) and a complex is -wave component. It can be clearly seen that both complex subdominant order parameters makes $YBa_2Cu_3O_{7-\delta}$ fully gapped. From [16]

3

The Single Electron Transistor as a Spectroscopic Tool for Investigating the order parameter in $YBa_2Cu_3O_{7-\delta}$

3.1 Basic working mechanisms of a Single Electron Transistor

A Single electron transistor (SET) consists of the same building blocks as a normal regular transistor. Current flows from a source to a drain region through a channel, or island, the gate voltage controls the current flow. But while regular transistor carry large currents in the ON-state, SETs aim at controlling a very small current, which involves single electron transport. This can be achieved if the channel, or island, is isolated from the source and drain by tunnel barriers whose tunnel resistance is higher than the quantum resistance, and at sufficiently low temperatures, so that the thermal energy is much lower than the charging energy of the system. By tuning the gate voltage, V_g , the total charge on the island can be controlled and the transport through the SET will be due to single electron tunnelling in and out of the island. An SET can be used as a spectroscopic tool to probe the energy levels of the island, including the superconducting gap. A detailed description is given below.

3.1.1 Principles of operation

A schematic representation of a SET is given in figure 3.1. It consist of a mesoscopic island and a source, drain and gate electrode. The island is connected with source and drain through tunnel barriers, and is capacitively coupled to the gate.

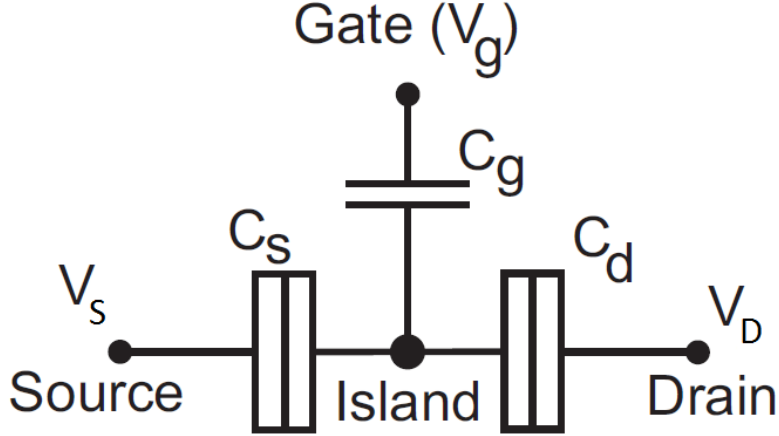


Figure 3.1: The circuit representation of a SET. Source and drain are coupled to the island by tunnel junctions, while the coupling between island and gate is purely capacitively. From [16]

The total energy of the island is the sum of the electrostatic energy, U , of the island and the work done by the voltage sources when an electron tunnels through a junction j , W_j [39].

$$U = \frac{1}{2C_\Sigma} \left(\sum_{i=1,2,3} \sum_{k>i} C_i C_k (V_i - V_k)^2 + (ne)^2 \right)$$

$$W_j = -e \sum_{i=1,2,3} (V_j - V_i) \frac{C_i}{C_\Sigma}$$

with C_i, C_k the capacitance of the junction, V_i, V_k the voltage over the junction and $C_\Sigma = C_S + C_D + C_g$ the sum of the capacitances, and can be expressed as follows:

$$E(n, V_g) = U + \sum_{i=1,2,3} n_j W_j \quad (3.1)$$

The excess charge on the island, n , can be controlled by tuning V_g, V_S and V_D . If the source-drain voltage is zero and for fixed gate voltage, the previous equation can be rewritten to:

$$E(n, n_g) = E_c (n_g - n)^2 \quad (3.2)$$

with $n_g = C_g V_g / e$ the gate induced charge, and neglecting a constant term that does not depend on n or n_g . The energy dependence on n_g thus consist of a set of energy parabola, shifted from one other by n_g for increasing excess charge n , as illustrated in 3.2a). Upon sweeping the gate voltage, the total energy of the island reaches a degeneracy point where two energy parabolas cross. Further increasing the gate voltage will

cause the tunnelling of an electron, so that the island can remain in its lowest energy state.

For non-zero source-drain voltage, the equations becomes more complex and will not be discussed in detail here. It suffices to say that there exist a threshold voltage for tunnelling to occur and this threshold is dependent both on the excess charge on the island, the applied gate voltage and the direction of tunnelling. Combined, this gives rise to the typical stability diagram of a SET with Coulomb diamonds. These are regions for certain V_{DS} and V_g where no tunnelling occurs and the excess charge on the island is quantized.

If the island and/or electrodes are superconducting, the presence of a the superconducting gap in the quasiparticle density of states needs to be taken into account. At zero temperature, a current through an NIS or SIS junction can only occur if the applied voltage overcomes the presence of the superconducting gap in the density of states, and must thus be greater than Δ or 2Δ respectively. To take the superconducting gap into account, the electrostatic energy in equation 3.1 needs to be modified with the free energy term F . For low temperatures and an isotropic gap, this free energy term can be written as: $F \sim \Delta - k_B T \ln(N_{eff})$, with N_{eff} the number of quasiparticle states in the island above the gap within thermal energy $k_B T$. In case the gap is isotropic without nodes, the free energy of the island implies the existence of a parity effect at very low temperatures. Adding two excess electrons to the island will require less energy, as they can form a Cooper pair and occupy a state at the Fermi energy level, while a single electron has to occupy a quasiparticle excitation state above the gap, which has an higher energy. This can be expressed by writing the free energy term as $p_n F$, with $p_n = 0$ for an even number of excess electrons, and $p_n = 1$ if n is odd. The equation 3.2 for a superconducting island can thus be rewritten as:

$$E(n, n_g) = E_c(n_g - n)^2 + p_n F \quad (3.3)$$

The energy parabola for the odd number of excess charge is lifted by F with respect to the even number of excess charge energy parabolas, as is illustrated in figure 3.2. This parity effect is clearly visible for SET with an island made of Al, and was first demonstrated by Tuominen et al. in 1992 [41]. It is important to note that the parity effect can be destroyed by quasiparticle poisoning, which for example happens in Nb SET. Here, tunnelling of an excess electron to the island occurs faster than 2 excess electrons can form a Cooper pair and relax to the Fermi energy level. Thus the parity effect is not observable.

The parity effect also affects the current-voltage characteristics of the SET. The source-drain current I_{DS} as a function of the gate induced charge n_g is illustrated in figure 3.3a) for a normal metal island and low, non-zero source-drain voltage V_{DS} . It consist of periodically distributed spikes with the period equal to the electron charge, e . The spikes in the current occur for gate voltages where the energy parabola cross and tunnelling occurs, which happens with e -periodicity for a NININ SET at n_g equal to half integer values, as seen in figure 3.2a). However, for a superconducting island, the parity effect has to be taken into account. The resulting source-drain current as a function of the

3.1. BASIC WORKING MECHANISMS OF A SINGLE ELECTRON TRANSISTOR

gate induced charge for small non-zero voltage for a superconducting island is shown in figure 3.3b). As the energy parabola are now lifted for odd values of excess electrons, the cross over is no longer situated for half-integer values of n_g . In addition, the periodicity is now $2e$, since the crossover of odd n parabola to even n parabola happens every time two excess electrons are added and similarly for the crossover of even n parabola to odd n parabola, as can be seen in figure 3.2b). The presence of the $2e$ periodicity is a clear indication of the parity effect and thus the superconducting gap.

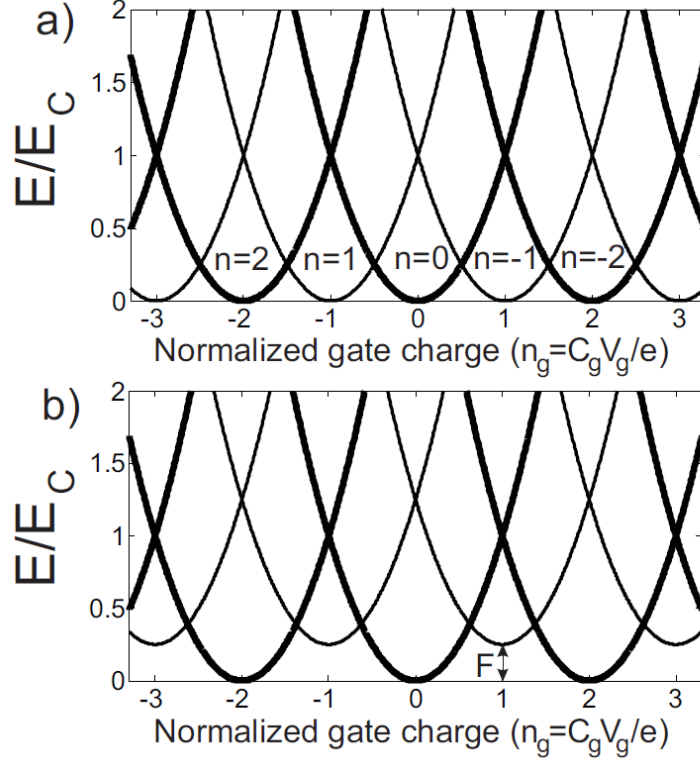


Figure 3.2: A comparison between the energy parabola for a SET with a normal (a) and superconducting (b) island. Each parabola represents the total energy on the island for a certain amount of excess electrons n . Tunneling occurs at the crossing of the parabola. For odd n , the parabolas are lifted by F for a superconducting island. From [16]

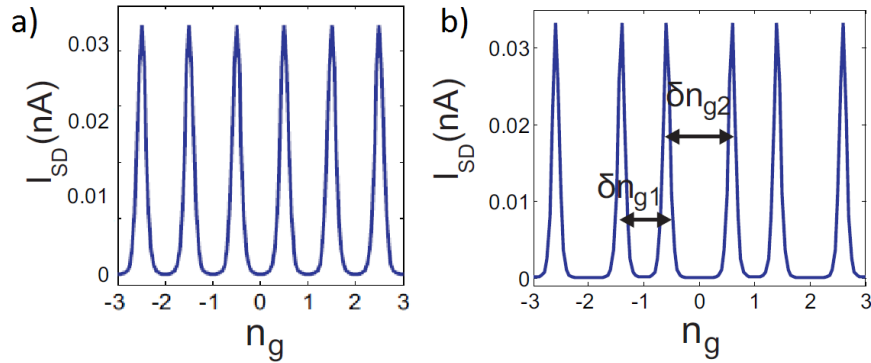


Figure 3.3: A comparison between the source-drain current I_{DS} as a function of the gate induced charge n_g for a small non-zero source-drain voltage characteristics between two SET, one with normal island (a) and the other with a superconducting island (b)). The periodicity of the current peaks is e and $2e$ respectively.

In order to obtain a good control over the current flowing through the SET, two important requirements need to be fulfilled. Firstly the tunnel resistance R_T of the tunnel junctions needs to be higher than the contact resistance R_Q . Secondly, the charging energy of the island $E_c = \frac{e^2}{2C_\Sigma}$ needs to be higher than the thermal energy $k_B T$, with $C_\Sigma = C_S + C_D + C_g$.

The second requirement is easily understood in terms of preventing thermal fluctuations to smear out the quantized charge on the island. In order to tunnel from the source to the island, the energy of the electron needs to be higher than the charging energy of the island. Good control over the current and charge on the island is achieved if that energy is provided by the applied source-drain voltage and gate voltage. As the thermal energy of the electron increase, the control over the SET decreases, as the electron gains finite probability to tunnel for gate voltages lower than the threshold voltage at zero temperature.

The first requirement can be easily derived as follows. The charging energy E_c must exceed the quantum energy uncertainty ΔE to be observable. Thus $E_c = e^2/(2C_\Sigma) \geq \Delta E$ and the energy uncertainty: $\Delta E \geq \hbar/(\Delta t) \approx \hbar/(RC)$. From these, we can write that the following condition must be met for the tunnel resistance: $R_T = 2\hbar/(e^2) \approx R_Q = 12\text{kOhm}$ [39].

While the second requirement is in principle achieved by reducing the dimensions of the island and of the tunnel barrier to the nanoscale, the first one is more stringent and requires some engineering of the interface between source-island and island-drain.

3.2 Experimental Observation of sub-dominant order parameter in all $YBa_2Cu_3O_{7-\delta}$ SET

Since an SET can be used to investigate the superconducting gap of the superconducting island, it is a useful tool to investigate the symmetry of the order parameter in HTS. Superconductivity in HTS is predominately a d-wave, characterized by nodal lobes. However, if a imaginary subdominant order parameter exists, the superconducting gap is present everywhere. Thus, the absence or presence of the parity effect in a HTS SET could prove in principle the absence or presence of the subdominant complex order parameter.

Gustaffson, D. et al. [17][16] made an all $YBa_2Cu_3O_{7-\delta}$ SET for this purpose, as is illustrated in figure 3.4. Source, drain, island and gate were made of $YBa_2Cu_3O_{7-\delta}$, with grain boundaries (GB) between the island and the source and drain electrode acting as tunnel junctions. These grain boundaries were created by depositing $YBa_2Cu_3O_{7-\delta}$ on a MgO(110) substrate, with a patterned SrTiO₃ strip on top of the MgO. $YBa_2Cu_3O_{7-\delta}$ grows epitaxially on both substrates but with a different relative orientation with respect to each other. The grain boundaries between source, island and drain acted as tunnel barriers. The orientation was such that the lobe of the order parameter in the source and drain pointed at the node in the island. For these 45° interfaces, mid gap states

are naturally formed in the absence of a subdominant order parameter. Thus no parity effect would be observable if the subdominant order parameter was not present. However, parity effect was observed in this SISIS $YBa_2Cu_3O_{7-\delta}$ SET, indicating the existence of the subdominant complex order parameter.

The exact symmetry of the subdominant order parameter is still unknown. In addition,

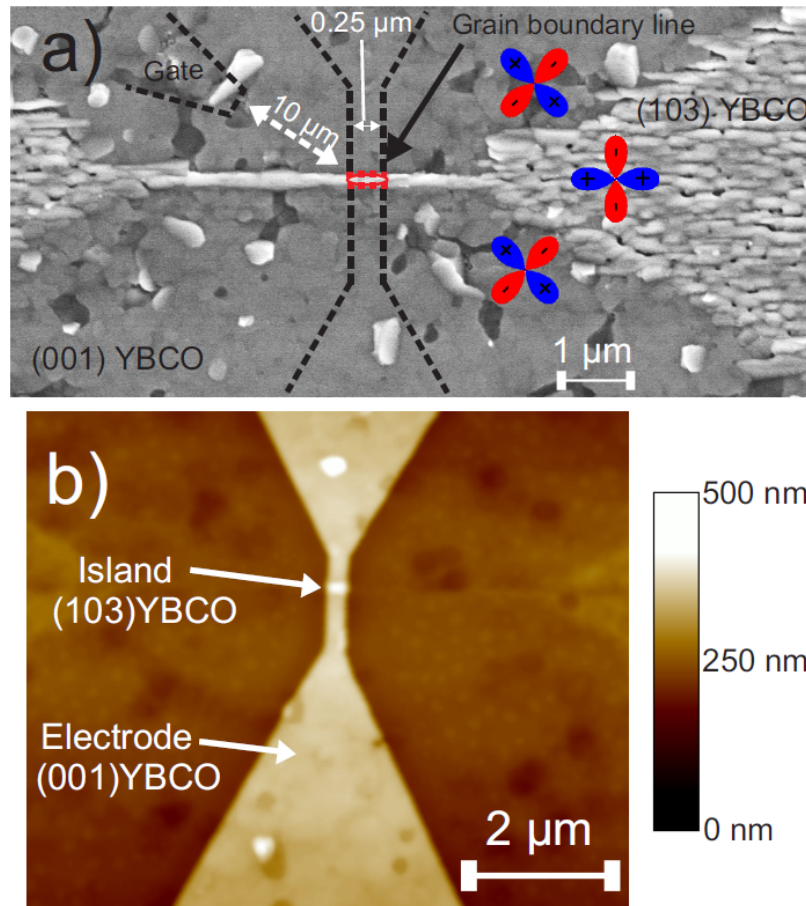


Figure 3.4: A SEM image of the $YBa_2Cu_3O_{7-\delta}$ film deposited on the patterned STO/MgO layer is given in a). The different orientations of the $YBa_2Cu_3O_{7-\delta}$ film are clearly visible. The orientation of the d-wave order parameter in the different regions is illustrated. The mask structure used to fabricate the SET is indicated by dashed lines. An AFM image of the fabricated final SET is given in b). From [16]

it is unclear if the subdominant order parameter nucleates at the surface or is a bulk phenomenon. Due to the fabrication process of the SET, the $YBa_2Cu_3O_{7-\delta}$ was also in the underdoped region. There are still a lot of open questions about the symmetry, size and doping dependence of the subdominant order parameter.

3.3 Follow-up Research

Clearly, there is a lot more to learn about the order parameter. Both doping and size dependence would be very interesting to explore, as well as the symmetry of the subdominant order parameter. However, the previous fabrication technique has quite some limitations in controlling and varying the doping, since it is rather difficult to change in a reproducible way the doping in both the electrodes and the island, as they have different orientations, and maintain the quality of the grain boundary tunnel junctions. In order to investigate the doping dependence, a new layout is needed. Instead of using $YBa_2Cu_3O_{7-\delta}$ also as electrodes, one could make an NISIN SET with normal instead of superconducting electrodes. One can then vary the doping of the $YBa_2Cu_3O_{7-\delta}$ island without affecting the electrodes. Since grain boundaries can not be used any more to achieve a high enough tunnel resistance, thus a tunnel barrier between the normal metal and $YBa_2Cu_3O_{7-\delta}$ needs to be engineered.

4

Engineering the Tunnel Barrier for a NISIN $YBa_2Cu_3O_{7-\delta}$ Single Electron Transistor

4.1 Motivation behind the thesis project

Despite years of research, there is still no satisfactory theoretical explanation of the superconductivity in high temperature superconductors, as stated in section 2.4.1. It is widely established that the superconducting order parameter in $YBa_2Cu_3O_{7-\delta}$ has a d-wave symmetry. However, the existence of a subdominant complex order parameter in $YBa_2Cu_3O_{7-\delta}$ was recently experimentally shown in the underdoped region, using an all $YBa_2Cu_3O_{7-\delta}$ SET [17], as explained in section 3.2.

The two main aspects which are of particular interest now are the doping dependence and how the subdominant order parameter changes with increasing/decreasing size of the $YBa_2Cu_3O_{7-\delta}$ island. Changing the size of the $YBa_2Cu_3O_{7-\delta}$ island can be done in a fairly straightforward way. The only care that has to be taken is that the two requirements for a working SET (tunnel resistance larger than the quantum resistance and the total charging energy must be lower than the thermal energy) are still fulfilled upon increasing the size of the island, since both the capacitance and the tunnel resistance are size dependent. However, investigating the doping dependence will be more difficult. It is not possible to control both the doping of the island and electrodes of this all $YBa_2Cu_3O_{7-\delta}$ SET while maintaining the quality of the grain boundaries between them, which are acting as the tunnel barriers. Thus a new design for the SET is needed. The proposed new design consists of a $YBa_2Cu_3O_{7-\delta}$ island, with normal metal source, drain and gate electrode. Changing from a SISIS SET to a NISIN SET is necessary to investigate the doping dependence. In addition, using electrodes made of other superconducting materials is also not possible. Using other HTS for source and drain is not

technically feasible. A normal metal source and drain electrodes is the best option. Noble metals like Pt, Au and Ag have been shown to be excellent capping layers for $YBa_2Cu_3O_{7-\delta}$ and do not alter its stoichiometry, making them a good choice as electrodes [36]. Unfortunately, these noble metals also make very good contact with $YBa_2Cu_3O_{7-\delta}$, resulting in a very low contact resistance around 10^{-7} to 10^{-8} Ohmcm² [31]. Clearly, the first step towards a new NISIN SET which could be used to investigate the subdominant order parameter, is the engineering of the interface between normal metal and $YBa_2Cu_3O_{7-\delta}$ to have a sufficiently high tunnel resistance, which will be the focus of this master thesis.

4.2 Methods to Engineering the interface Au-YBa₂Cu₃O_{7-δ}

This master thesis aims at engineering the interface between $YBa_2Cu_3O_{7-\delta}$ and the noble metals Au and Pt, in order to achieve a suitable tunnel barrier for a NISIN SET, that can be used to investigate the subdominant complex order parameter. Au is chosen since it is a noble not-superconducting metal, and as such does not react with the $YBa_2Cu_3O_{7-\delta}$ while protecting it. In addition, it is easy to work with. Pt is used as a sticking layer since Au does not have good adhesion to the side of $YBa_2Cu_3O_{7-\delta}$ wires. The creation a tunnel barrier between superconductor-normal metal can be done in two ways.

The first method, and most common, is the growth of an thin oxide layer on top of the $YBa_2Cu_3O_{7-\delta}$. While widely used with LTS superconductors to fabricate SETs with very good control over the properties, this method is not advisable for HTS for two reasons. First, $YBa_2Cu_3O_{7-\delta}$ has no natural oxide that can be grown by supplying oxygen and heat. Secondly, the deposition of an oxide is done by sputtering the metal ions in an reactive oxygen environment. As such, the metal ions will just as easily react with the oxygen atoms present in the $YBa_2Cu_3O_{7-\delta}$, forming an oxygen depletion layer at the surface, which limits our control over the doping of $YBa_2Cu_3O_{7-\delta}$ at the surface layer. This is shown by Suzuki, Y. et al [36] for Sn and Al. The surface of $YBa_2Cu_3O_{7-\delta}$ in contact with Al and Sn was shown to be depleted in oxygen by X-ray photo-electron spectroscopy, which was not the case for the noble metals Ag and Au, which do not oxidise. Similar results were found by Gao et al. for Fe [15] and Oshima et al. for Si [31]. Therefore, creating an oxide layer by reactive oxygen metal ion sputtering while maintaining control over the doping of the surface of the $YBa_2Cu_3O_{7-\delta}$ island might not be feasible. It might however be possible to grow insulating barrier of MgO, CeO₂, LaAlO₃ or SrTiO₃ as there are chemically compatible with $YBa_2Cu_3O_{7-\delta}$ and are deposited as molecular clusters and thus will not leech oxygen from $YBa_2Cu_3O_{7-\delta}$. Most of them are also used as substrates for $YBa_2Cu_3O_{7-\delta}$ deposition. The deposition of these materials is however challenging, requiring high temperatures and oxygen pressure. The second approach involves the damaging of the $YBa_2Cu_3O_{7-\delta}$ surface, thus creating a thin amorphous layer at the surface, below which a stoichiometric $YBa_2Cu_3O_{7-\delta}$ surface should be preserved. The damaging can be done by chemical treatment of the

surface with an acid or base, or by mild ion etching. Chemical treatment is less advisable, since it is difficult to achieve precise control over the reaction parameters to obtain uniform barriers. Mild ion etching on the other hand should be easier to control and allow for a more reliable fabrication. The etching time and etching voltage can be easily tuned and hopefully the etching would not effect to doping of the $YBa_2Cu_3O_{7-\delta}$.

In this thesis, we will study at the nanoscale the effect of mild ion etching on the surface of $YBa_2Cu_3O_{7-\delta}$ with the aim to create a Au-(or AuPt)-I- $YBa_2Cu_3O_{7-\delta}$ NIS tunnel junction with a tunnel resistance higher than the quantum resistance.

4.3 Outline of experimental work to investigate the Au(or Pt)- $YBa_2Cu_3O_{7-\delta}$ interface and the effect of mild ion etching

The interface properties will be investigated by fabricating nanoscale Au- $YBa_2Cu_3O_{7-\delta}$ junctions with the $YBa_2Cu_3O_{7-\delta}$ having undergone mild Ar ion etching before Au deposition on the top and Pt-Au deposition on the side of the $YBa_2Cu_3O_{7-\delta}$ nanowires. The etching voltages will be varied, as well as the etching times.

The IV characteristics will be measured for these junctions and tunnel characteristics and contact resistivity between Pt- $YBa_2Cu_3O_{7-\delta}$ and Au- $YBa_2Cu_3O_{7-\delta}$ extracted. The contribution from side and top contact can be differentiated. The details of the device layout, fabrication process, measurement set-up and the results are given in chapter 6.

In order to gain more insight in how the ion milling affects the surface, the devices will be treated with ozon, since we assume that it replenishes any created oxygen vacancies in the $YBa_2Cu_3O_{7-\delta}$ surface and bulk. We also believe that ozonation helps to restore the superconducting state, and might affect the interface properties. Measuring the contact resistance, critical current and current-voltage characteristics will give an indication of how mild etching changes the $YBa_2Cu_3O_{7-\delta}$ interface properties. The results can found in chapter 7.

5

Tunneling characteristics of normal metal - insulator - superconductor junctions

This section aims at giving an overview of the tunnelling characteristics of metal-superconductor junctions that we will use as a guidance for the interpretation of the conductance spectra of our NIS junctions. The IV characteristics of a normal metal-superconductor junction are very dependent on the transparency of the tunnel barrier between the normal metal and superconductor. In addition, the d-wave symmetry and 2D dimensionality of the cuprates add extra complexity to the tunnelling spectrum and has to be taken into account.

5.1 Metallic and tunnelling characteristics of normal metal-LTS superconductor junctions

Two extreme regimes can be differentiated in normal metal-superconductor junctions, depending on the strength/transparency of the barrier between the metal and the superconductor. If a very strong barrier is present (low transparency), the IV characteristic has the conventional features of a tunnel NIS junction. For a very weak barrier (high transparency), the junction will behave in a metallic like way and is denoted as NS. In addition, Andreev reflection plays a major role in this case. In both cases, the presence of the superconducting gap and supercurrent greatly influences the IV characteristics.

5.1.1 IV characteristics of a NIS junction

For a very strong barrier, like an thin insulating layer between the normal metal and superconductor, current can only flow by electrons tunnelling one by one through the barrier. Electrons can only tunnel from an occupied state on one side of the insulator to an empty state on the other side of the insulator at the same energy level. However the density of quasiparticle excitations in a superconductor is gapped. Thus for a NIS junction at zero temperature, electrons can only tunnel through the barrier for an applied voltage bias bigger than the gap energy: $eV \geq \Delta$, as illustrated in figure 5.1. This results in the conventional tunnel features in the IV characteristics, as illustrated in figure 5.3. No current flows for voltage smaller than Δ/e , for higher voltage, the electrons start tunnelling and the IV curve is linear with the slope corresponding to the normal tunnel conductance. For higher temperatures in a NIS, empty states higher than the Fermi level will be occupied according to the Fermi distribution function, which allows tunnelling in the NIS junction for applied voltage bias smaller than the gap energy, as is also illustrated in figure 5.3.

It is important to note that due to the isotropic gapped superconductivity in metals, the typical NIS IV characteristics does not depend on the orientation of the normal and superconducting electrodes with respect to each other. This will not be the case for HTS. Here the IV characteristics can be orientation dependent, as the gap is not isotropic.

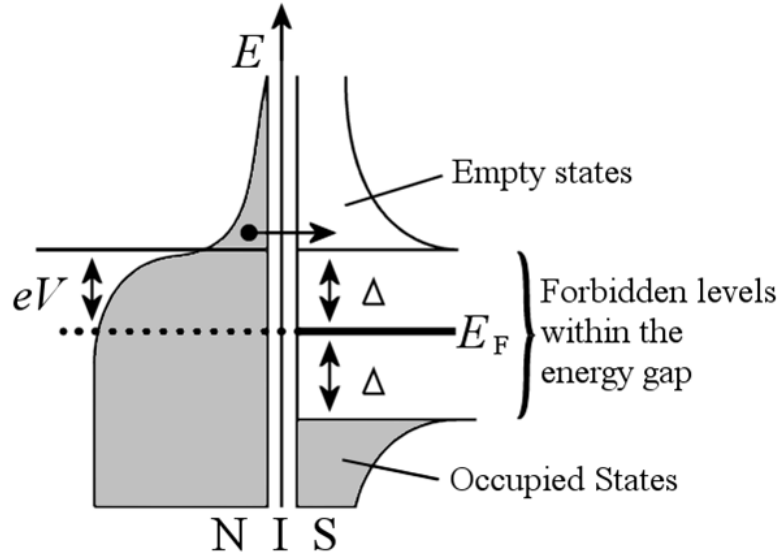


Figure 5.1: An illustration of a NIS tunnel junction. Quasiparticles can only tunnel through the barrier if the applied voltage is bigger than the gap energy.

5.1.2 IV characteristics of a NS junction

For a high transparency interface between the normal metal and superconductor, current will occur for applied voltages smaller than the gap energy due to Andreev reflection

at the interface [1]. An illustration of the mechanism of Andreev reflection is given in figure 5.2. An incident electron coming from the normal metal with an energy smaller than Δ , is transmitted through the interface as a Cooper pair and a hole is reflected back. For higher energies, the electrons in the metal can flow to empty states above the superconducting gap in the superconductor, in addition to the Andreev reflection current. Thus for sub-gap applied voltages, the current is carried by Cooper pairs in the superconductor, and for voltages higher than the gap it is carried by both quasi-particle excitations, similar to the NIS case and Cooper pairs.

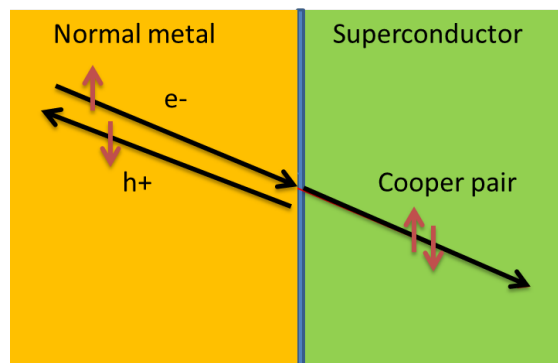


Figure 5.2: An illustration of the Andreev reflection at the interface.

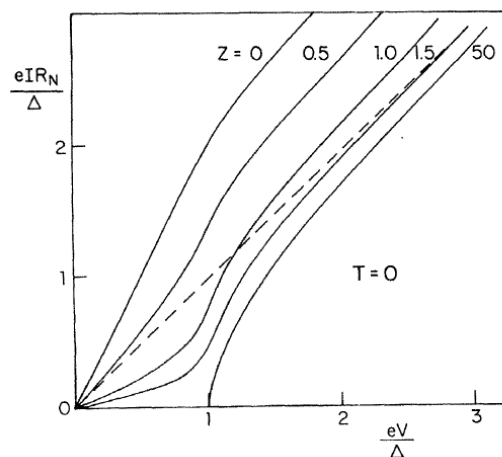


Figure 5.3: IV characteristics of a NS junction for various barrier strengths Z at $T = 0$. The dashed line gives the normal-state curve. From [8]

	A	B
Normal state	0	$\frac{Z^2}{1 + Z^2}$
Superconducting state		
for $E < \Delta$	$\frac{\Delta^2}{E^2 + (\Delta^2 - E^2)(1 + 2Z^2)^2}$	$1 - A$
for $E > \Delta$	$\frac{u_o^2 v_o^2}{\gamma^2}$	$\frac{(u_o^2 - v_o^2)^2 Z^2 (1 + Z^2)}{\gamma^2}$

Table 5.1: The analytical expressions for the probabilities of Andreev reflection (A) and normal reflection (B) at a NS interface, as a function of the barrier strength Z for different states and energies. $u_o = 1 - v_o = 1/2[1 + \sqrt{\frac{E^2 - \Delta^2}{E^2}}]$. From [8]

5.1.3 Bridging the two regimes, the BTK approach

Blonder, Tinkham and Klapwijk [8] gave a theoretical model for normal metal-superconductor junctions in which the barrier strength is a tunable variable. By changing the barrier strength, they could reproduce both the NS and NIS IV characteristics, as well as for intermediate barrier strengths. An electron coming from the normal metal can undergo Andreev reflection at the interface, can reflect normally or can be transmitted with or without branch crossing. The probabilities of these 4 different possibilities are denoted by A, B, C and D. Since the sum of all probabilities is one, $A + B + C + D = 1$, and we are not interested in differentiating between branch crossing and not branch crossing, knowing $A(E)$ and $B(E)$ for all possible barrier strengths Z results in complete information of the current-voltage characteristics and the shape of the conductance spectra at low temperatures, as $C + D = 1 - A - B$. The following expression for the total current through a NS junction holds for all barrier strengths [8]:

$$I_{NS} = 2N(0)e v_F A \int_{-\infty}^{\infty} (f_o(E - eV) - f_o(E))(1 + A(E) - B(E))dE \quad (5.1)$$

$A(E)$ and $B(E)$ can be expressed as a function of Z, the dimensionless barrier strength, as given in table 5.1. The current voltage characteristics of a NS junction for different values of the barrier strength Z obtained by this model are given in figure 5.3. A perfect transparent NS interface corresponds to $Z = 0$. As the barrier strength increases, the current carried by the Andreev reflection clearly decreases to zero for a tunnel NIS junction, $Z \gg 1$. The probability of the Andreev reflection inside the gap region and of the transmission coefficients C and D outside the gap, as well as the probability of normal reflection B are given in figure 5.4 for varying barrier strength and as a function of the energy. This figure is very useful to analyse the conductance spectra, as the conductance is proportional to $1 + A - B$ as can be seen from equation 5.1, which can be rewritten

as: $1 + A - B = A + C + D$.

Inside the gap, the conductance is flat for very transparent interface due to the Andreev reflection. As the transparency decreases, A becomes peaked at $V = \Delta/e$ for intermediate barrier strength and drops to zero inside the gap for NIS interfaces. Outside the gap, the conductance spectra is determined by the transmission probabilities through the interface with and without branch crossing, D and C, which equals $1 - B$, and whose dependence on the energy and barrier strength can be seen in figure 5.4.

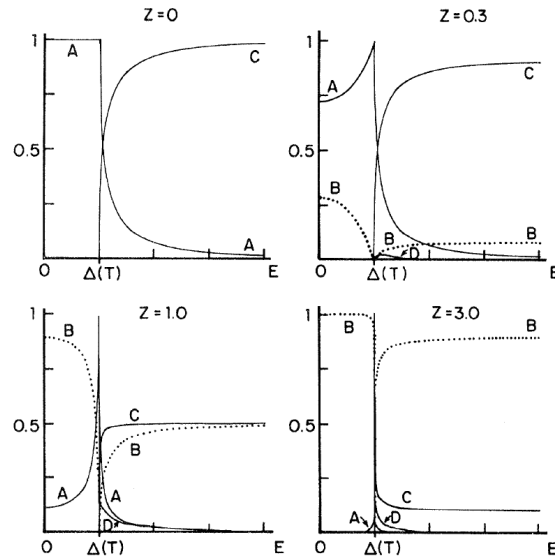


Figure 5.4: The probability of the Andreev reflection, normal reflection and transmission coefficients A, B C and D as a function of the applied voltage and for different barrier strengths Z. The sum of all probabilities equals one: $A + B + C + D = 1$. From [8]

5.2 Metallic and tunnelling characteristics of normal metal-HTS superconductor junctions

The BTK formalism, as derived by [8] and explain in section 5.1.3 assumes a s-wave superconducting order parameter to derive the equations for the Andreev reflection and normal reflection coefficients, $A(E)$ and $B(E)$ respectively, of incident electrons on the N-S interface. They are both depending on the barrier strength of the interface Z and the energy E of the incident electron.

However, the BTK tunnelling spectra cannot be directly used to interpret the HTS NS interface. With HTS, zero bias conductance anomalies, ZBCA are observed, there is a big difference between tunnelling along the a-b plane and tunnelling along the c-axis, and a linear or parabolic background of the conductance-voltage spectra is often observed. These differences can in part be attributed to the d-wave symmetry of the order parameter in the cuprates and the 2D layered structure of the material.

Tanaka and Kashiwaya expanded the BTK formalism to the d-wave symmetry valid for HTS [38]. The conductance becomes dependent on the angle θ , between the normal of the interface and the incident electrons, and the angle α , between the normal of the interface and the orientation of the d-wave order parameter (which depends on the specific orientation of the interfaces), as is illustrated in figure 5.5.

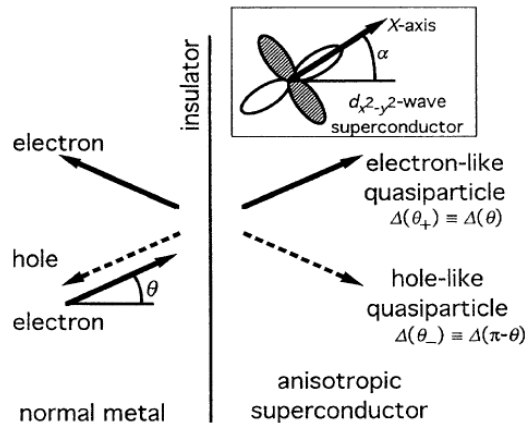


Figure 5.5: An illustration of the NS interface with the incident angle θ and the orientation angle α between the d-wave order parameter and the normal of the interface. The different reflection and transmission processes are also indicated. From [38].

For tunnelling along the a-b-plane and $\alpha = \pi/4$, a peak in the conductance at zero bias is observed, which is due to the difference in effective pair potential for electron and hole like quasiparticles. However, no ZBCP, is observed for tunnelling along the c-axis, since here the quasiparticles experience the same pair potential in all directions.

A comparison between the theoretical conductance characteristics for tunnelling in the c-axis direction and in the a-b plane is given in figure 5.6 for a strong interface barrier.

The difference between a-b plane tunnelling if the orientation angle of the order parameter α equals $\pi/4$ or zero is shown. A clear ZBCP is present for $\alpha = \pi/4$, while a more conventional tunnelling spectra is obtained for $\alpha = 0$. Tunnelling in the c-axis direction is characterized by a V shaped conductance curve in the gap region.

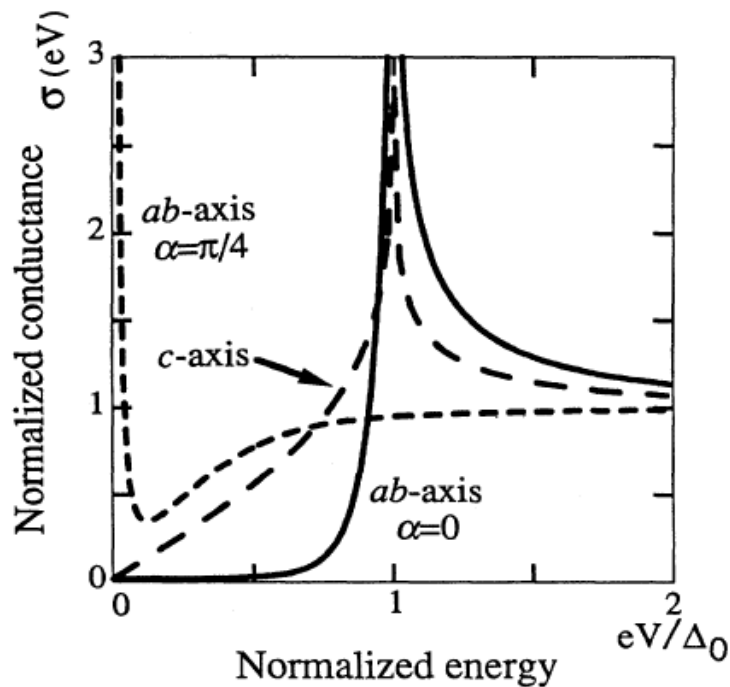


Figure 5.6: The calculated tunnel spectra of N-I- d-wave superconductor for c-axis and a-b plane tunnelling for $\alpha = \pi/4$ and $\alpha = 0$ and barrier strength $Z = 10$. From [20]

The dependence on the orientation angle α and the barrier strength Z of the conductance spectra is shown in figure 5.7. Clear gap features are recovered for high Z values and α angles close to zero. The ZBCP becomes sharper defined for higher barrier strengths Z and for α values closer to $\pi/4$. For comparison, the normalised bulk density of states is also plotted in the figure 5.7.

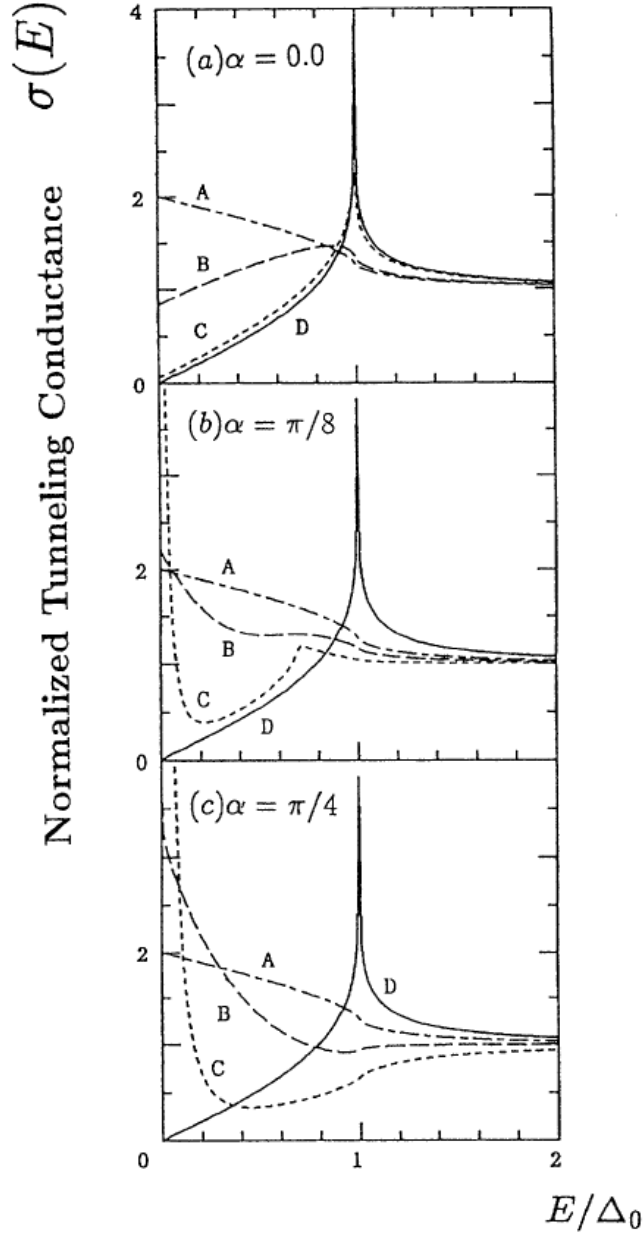


Figure 5.7: The calculated normalized tunnelling conductance in the a-b plane as a function of the energy for a N-I- d-wave superconductor. (a) $\alpha = 0$, (b) $\alpha = \pi/8$ and (c) $\alpha = \pi/4$. The different barrier strengths are denoted by A: $Z = 0$, high transparency, B: $Z = 1$, intermediate transparency, C: $Z = 5$, low transparency. The curve indicated by D is the normalised bulk density of states in a d-wave superconductor. From [38]

Kashiwaya [20] showed that the ZBCP is a consequence of the presence of mid gap states which can carry current. These mid-gap states are naturally formed for 45° degree

interfaces. In this case the junction can be seen more as a NIN'S junction rather than a NIS junction, with N' representing a HTS layer where the effective order parameter, encountered by the incident electron is zero.

Another interesting feature of the conductance spectra is the quasi linear increase of the conductance with high voltages, as illustrated in figure 5.8. This non-constant conductance can be attributed to inelastic scattering from states close to the barrier, as shown by Kirtley et al. in the case of a Al-Al₂O₃-Cr₂O₃-Pb junction [23]. The Cr₂O₃ in the oxide barrier causes inelastic scattering. By increasing its concentration in the barrier, the conductance background became more linear.

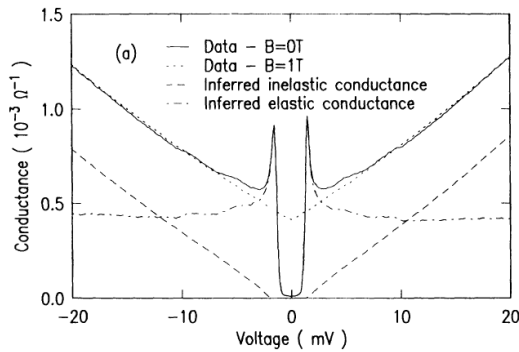


Figure 5.8: An illustration of the observed linear background due to inelastic scattering for a Al-Al₂O₃-Cr₂O₃-Pb junction. The dashed curve is the inelastic component, the dot-dashed line the elastic component to the total conductivity. Applying a magnetic field destroys the superconductivity, but the linear background remains. From [23]

To conclude, c-axis tunnelling results in a V-shaped conductance spectra, while for a-b plane tunnelling, there can be ZBCP in the gap region, with the peak height dependent on the barrier strength and the orientation angle α .

Gap features in $YBa_2Cu_3O_{7-\delta}$ are typically observed around 20mV for NIS junctions.

5.3 The Effect of an Inhomogeneous Superconducting Electrode

Both in LTS and HTS a thin normal layer can be present at the interface of the superconductor. This effectively changes the junction structure from NIS to NIN'S', with N'S' the superconductor base electrode, as is depicted in figure 5.9. This N'S' bilayer can be weakly or strongly coupled. In the latter case, the junction still behaves according to the BTK [8] theory as shown by Arnold [2].

If the N'S' bilayer is weakly coupled, substantial deviations from the BTK model can be observed, as shown by Chiara et al. [11]. In addition to the dimensionless barrier strength Z , they used two new parameters that characterised the bilayer. $\Gamma_{N'} = \alpha/d_{N'}$ is

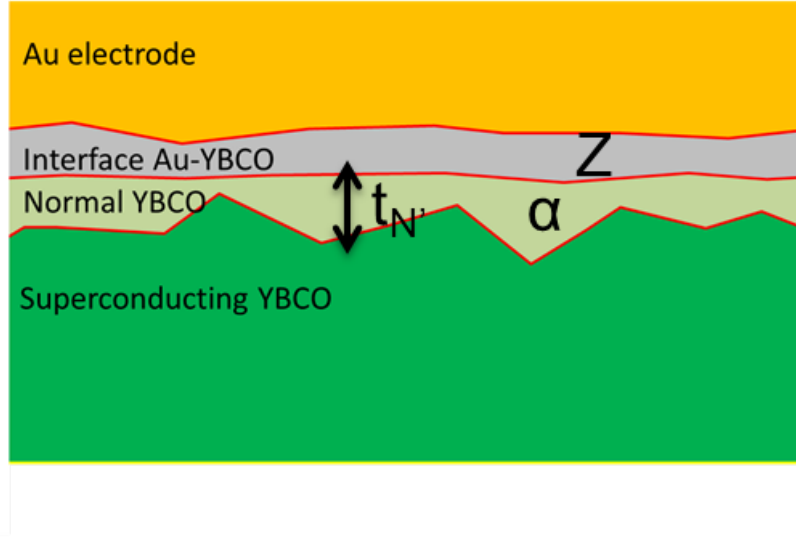


Figure 5.9: An cross section of the $\text{Au-YBa}_2\text{Cu}_3\text{O}_{7-\delta}$ interface with an inhomogeneous normal $\text{YBa}_2\text{Cu}_3\text{O}_{7-\delta}$ layer present at the interface.

the ratio between the transmission probability coefficient α of the N'S' interface and the thickness of the normal layer N'. Similarly, $\Gamma_{S'} = \alpha/d_{S'}$ is the ratio between α and the thickness of the superconducting layer. The N' is superconducting due to the proximity effect with S', if $\xi_{S'} > d_{N'}$, which introduces a gap $\Delta_{N'}$ in N'. Depending on the barrier strength Z and the thickness of N', $d_{N'}$, assuming α remains constant, the following ZBCA and conductance curves can be obtained.

The conductance as a function of the energy for a perfect interface, $Z = 0$ is shown in figure 5.10 for different values of $d_{N'}$, with the other parameters constant. As $\Gamma_{N'}$ decreases (thus $d_{N'}$ increases), the conductance shows larger deviations from the BTK predictions. There is no constant conductance in the gap if N' is present in the junction. Instead a ZBCP is observed, of which the height decreases with increasing $d_{N'}$. In addition, a bump at the gap energy is present, which disappears for increasing $d_{N'}$.

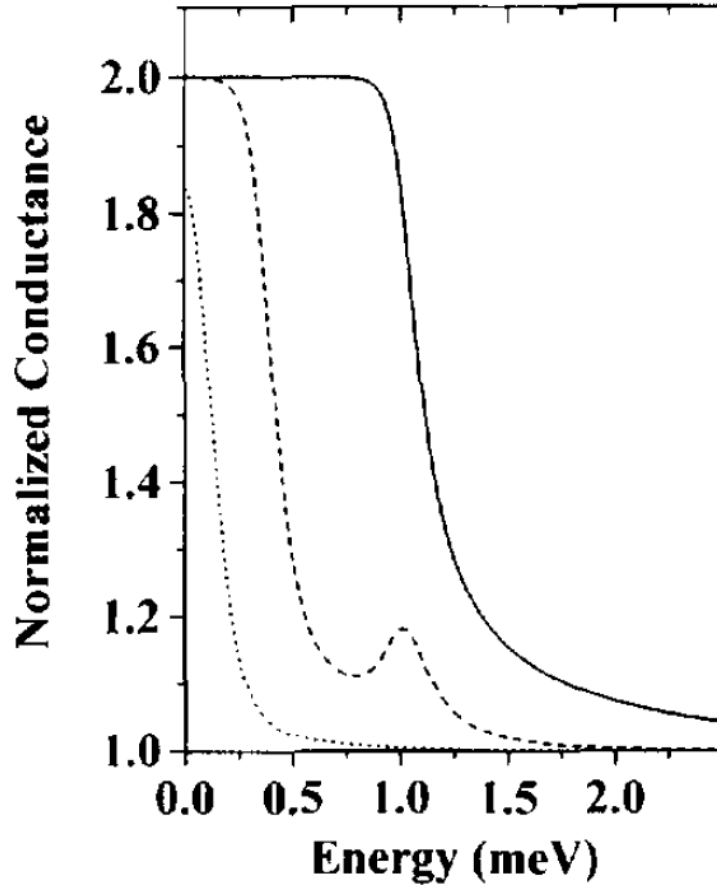


Figure 5.10: The calculated normalised conductance as a function of energy for a perfect NN'S' interface. $Z = 0$, $\Delta_S = 1\text{meV}$, $d_{N'} \ll d_{S'}$ (dashed line) or $d_{N'} \approx 5d_{S'}$ (dotted line). The predicted BTK conductance is indicated by a full line. From [37]

For higher barrier strength, the calculated conductance curves are shown in figure 5.11 for $Z = 0.5$ and 5.12 for $Z = 1.5$. For intermediate barrier strengths and thin normal layer, BTK like behaviour is observed, while as $d_{N'}$ increases, ZBCP are recovered. A bump around the gap energy is also present and disappears for increasing $d_{N'}$. For a stronger barrier $Z = 1.5$, BTK like behaviour is observed for a higher value of $d_{N'}$. As $d_{N'}$ increases more, a flat conductance spectrum is observed, with a small drop at zero bias.

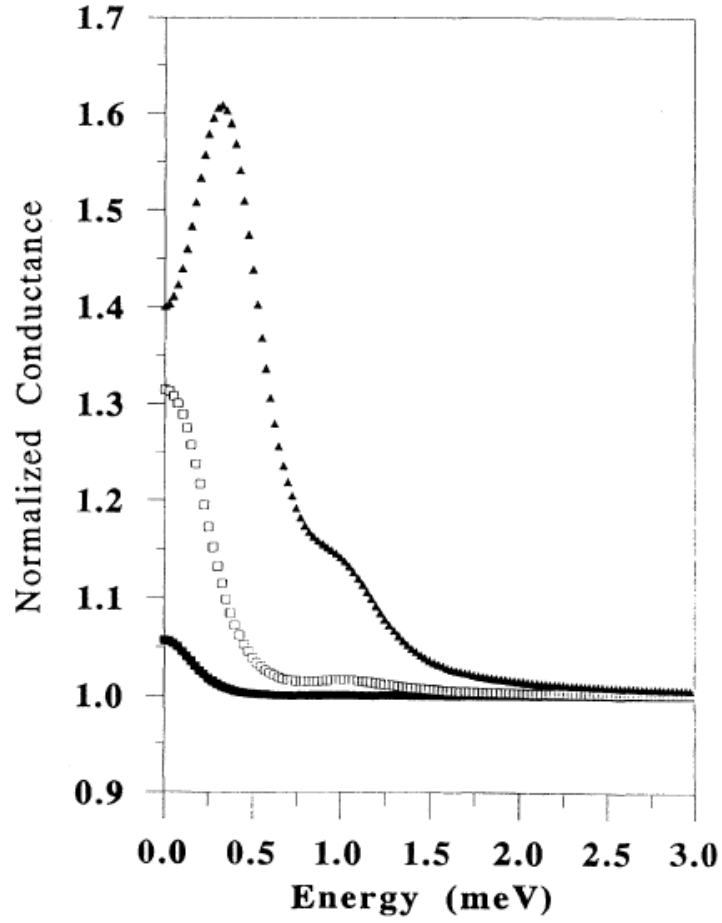


Figure 5.11: The calculated normalised conductance as a function of energy for intermediate barrier strength, $Z = 0.5$ for a NIN'S' junction. $\Gamma_S = 1$, $\Gamma_{N'} = 0.1\text{meV}$ (triangles), $\Gamma_{N'} = 0.05\text{meV}$ (squares) or $\Gamma_{N'} = 0.005\text{meV}$ (full squares). From [11]

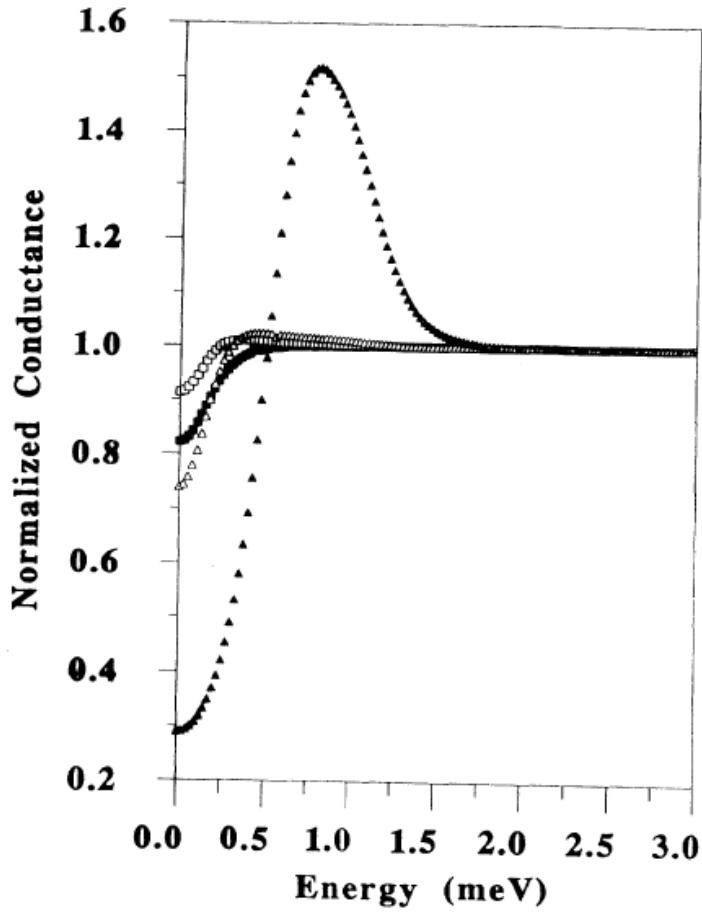


Figure 5.12: The calculated normalised conductance as a function of energy for high barrier strength, $Z = 1.5$ for a NIN'S' junction. $\Gamma_S = 1$, $\Gamma_{N'} = 0.5\text{meV}$ (full triangles), $\Gamma_{N'} = 0.1\text{meV}$ (triangles), $\Gamma_{N'} = 0.05\text{meV}$ (full squares) or $\Gamma_{N'} = 0.005\text{meV}$ (squares). From [11]

6

Device Layout, Fabrication Process and Measurement Set-up

6.1 Introduction

The mild ion milling of the $YBa_2Cu_3O_{7-\delta}$ surface needs to be optimised to create both a high enough tunnel barrier to get resistances higher than R_Q at the nanoscale and to keep the superconducting properties of $YBa_2Cu_3O_{7-\delta}$ as intact as possible. In order to investigate the effect of mild ion etching of the $YBa_2Cu_3O_{7-\delta}$ surface on the interface $YBa_2Cu_3O_{7-\delta}$ -Au, the IV characteristics of the Au- $YBa_2Cu_3O_{7-\delta}$ nanojunction need to be measured.

Previous research on $YBa_2Cu_3O_{7-\delta}$ -Au junctions always focused on the optimization of the interface to get a low contact resistance to engineer Josephson junction [31][42]. In addition, the junctions were always on the micro-size and the way of measuring did not allow to distinguish between the contact resistance in the a-b plane and that in the c-axis direction. Since the SET will be nano-sized, the junctions fabricated and studied here will also be nano-sized to study the possible size-dependence of the contact resistivity, as previously reported for μm sized junctions [42]. As it is very difficult to fabricate the SET such that the Au source and drain make only contact with one of the $YBa_2Cu_3O_{7-\delta}$ crystal orientations, the contact resistivity for interfaces parallel to the a-b plane and c-axis, respectively, will be investigated. This can be done by a clever engineered device layout. The fabricated Au- $YBa_2Cu_3O_{7-\delta}$ interface can behave as an NS junction or NIS junction.

After measuring, the samples will be exposed to an ozone treatment and remeasured. It is suspected that this treatment affects the superconducting properties of $YBa_2Cu_3O_{7-\delta}$.

6.2 Measuring the contact resistance: Concept and Device Layout

The following device was fabricated to measure the contact resistance between Au and $YBa_2Cu_3O_{7-\delta}$. It consists of 4 small $YBa_2Cu_3O_{7-\delta}$ nano-wires, laying in parallel with each other and at spaced $30\ \mu\text{m}$, $60\ \mu\text{m}$ and $90\ \mu\text{m}$ from each other respectively. A gold bar perpendicular to the wires connects them together. A schematic representation of the device is given in figure 6.3. The equivalent electrical circuit for two superconducting wires connected by a gold bar would consist of 3 resistors in series, namely, the contact resistance between the first wire and Au, the resistance of the gold bar and the contact resistance between the second wire and Au:

$$R_{tot} = R_{c_1} + R_{Au} + R_{c_2} = r_{Au}l + R_{c_1} + R_{c_2} \quad (6.1)$$

with R_c the contact resistance between $YBa_2Cu_3O_{7-\delta}$ and Au, R_{Au} the resistance of the gold bar, r_{Au} the resistance per unit length of the gold bar and l the length of the gold bar connecting the two wires, as can be seen in figure 6.3. As can be seen from equation 6.1, R_{tot} varies linearly with the length of the Au bar. By measuring the resistance between the different wires in all possible configurations (corresponding to the length of the gold bar being $30, 60, 90, 150, 180$ and $90\ \mu\text{m}$) and plotting the measured resistance as a function of the length between the wires, one could obtain in principle the contact resistance $R_{c_1} + R_{c_2}$ as the intercept of the y-axis in a linear fit of R_{tot} as a function of the length l . This plot is illustrated in figure 6.1 for three devices with different width of the $YBa_2Cu_3O_{7-\delta}$ wires.

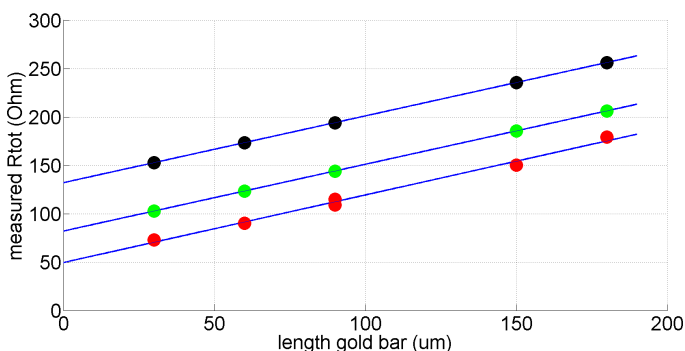


Figure 6.1: An illustration of how the obtained total resistance of the different configurations per device should scale with the corresponding length of the gold bar. The black dots correspond to the device with the smallest wires and the red ones to the biggest. The intercepts with the y-axis equals twice the contact resistance, $R_{c_1} + R_{c_2}$, for the different $YBa_2Cu_3O_{7-\delta}$ wires.

It is important to be able differentiate between the contributions of the top and the sides of the wires to the total contact resistance, as they involve the contact with the

different crystallographic planes of $YBa_2Cu_3O_{7-\delta}$. The superconducting and conductive properties of $YBa_2Cu_3O_{7-\delta}$ are highly anisotropic, as explained in section 5. This differentiation is done by fabricating 5 different devices on one sample, each device consisted of 4 wires of the same width and a perpendicular gold bar, as described above. The width of the wires varied between the different devices from 100nm to 500nm. As such, once the total contact resistance was obtained for each device (from the intercept of the linear fit in figure 6.1), the variation in the top area for the different total contact resistance $R_c^{tot} = R_{c1} + R_{c2}$ could be used to differentiate between the top and side contact resistance, R_c^{side} and R_c^{top} . Assuming that the total contact resistance can be modelled by 3 resistors in parallel, the top contact resistance and two times the side contact resistance as illustrated in figure 6.4, the total contact conductance can be written as:

$$G_c^{tot} = 2G_c^{side} + G_c^{top} = 2G_c^{side} + g_c^{top} A \quad (6.2)$$

with G_c^{side} the contact conductance of the side, G_c^{top} the contact conductance of the top, g_c^{top} the contact conductivity of the top per unit area of the top and A the area of the top contact. The side contact conductance can be extracted from the intercept of the linear fit of G_c^{tot} as a function of the top area. The slope of the linear fit corresponds to the contact conductivity of the top per unit area. This plot is illustrated in figure 6.2.

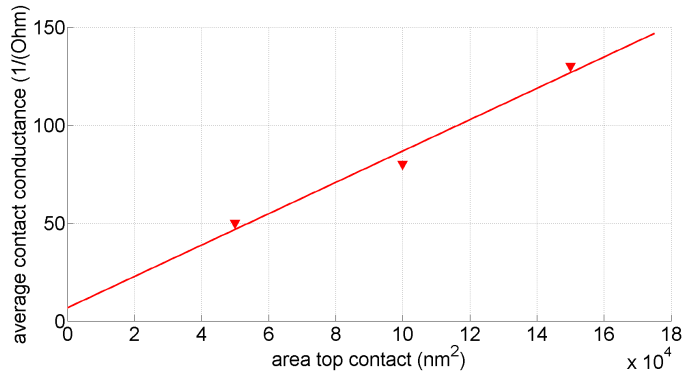


Figure 6.2: An illustration of how the obtained total contact conductance of the different configurations per device should scale with their corresponding top contact area.

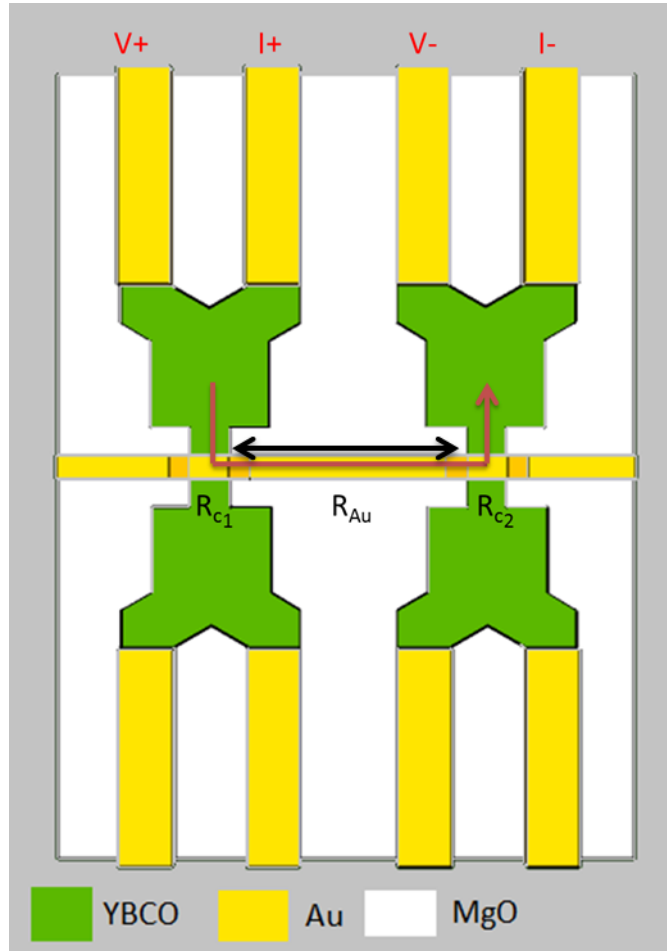


Figure 6.3: A schematic representation of part of the device. It consists of two $YBa_2Cu_3O_{7-\delta}$ wires, connected by a gold bar. The wires are connected to 4 electrodes, to allow for 4-point measurements. The red arrow indicates the current through the device. The 3 resistances in series it encounters are indicated, as well as the length of the gold bar.

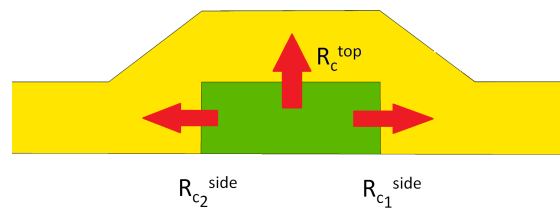


Figure 6.4: The cross section between the $YBa_2Cu_3O_{7-\delta}$ nano-wire, connected to the gold bar. The three different resistances, R_{c1}^{side} , R_{c2}^{side} and R_c^{top} are indicated. The red arrows represent the current going from the $YBa_2Cu_3O_{7-\delta}$ wire to the gold bar.

The $YBa_2Cu_3O_{7-\delta}$ wires are connected to 2 $YBa_2Cu_3O_{7-\delta}$ pads on each side, which will be used to connect to the electronics to perform the 4 point measurements. These pads have gold on top to facilitate the wire bonding. It is important to note that the gold layer does not cover all the $YBa_2Cu_3O_{7-\delta}$ electrodes, the layer stops before the two electrode join together and form the $YBa_2Cu_3O_{7-\delta}$ nano-wire, as is illustrated in figure 6.3.

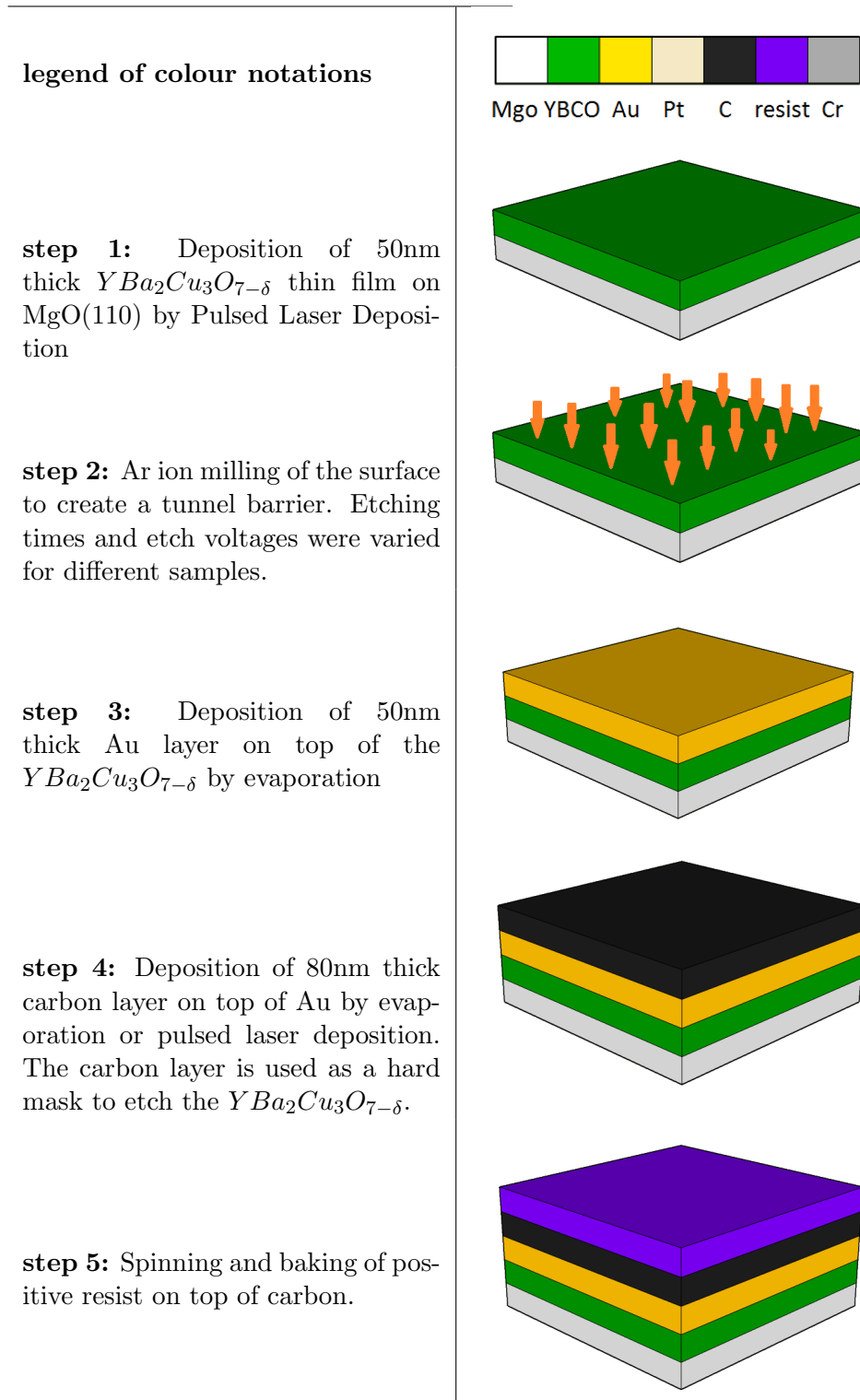
6.3 Fabrication process

$YBa_2Cu_3O_{7-\delta}$ is a difficult material to work with as its superconducting properties depend heavily on the deposition process, subsequent process steps, contamination and loss of oxygen. Therefore $YBa_2Cu_3O_{7-\delta}$ films need to be protected with an inert capping layer deposited in situ, which is usually a noble metal. In addition, unlike LTS, $YBa_2Cu_3O_{7-\delta}$ nanostructures cannot be created using a traditional liftoff process because of the high deposition temperature (750°) of HTS thin films.

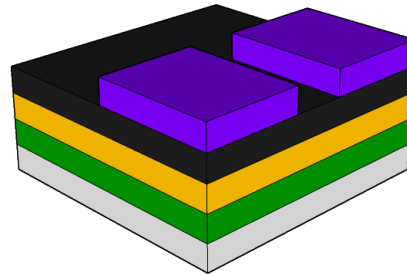
To create $YBa_2Cu_3O_{7-\delta}$ nanostructures, one deposits first the $YBa_2Cu_3O_{7-\delta}$ thin film, protects it with a thin Au layer and then patterns a mask on top of the $YBa_2Cu_3O_{7-\delta}$ -Au film. The $YBa_2Cu_3O_{7-\delta}$ -Au film is then locally etched away, which is typically done by Ar ion milling.

The device layout for investigating the Au- $YBa_2Cu_3O_{7-\delta}$ interface has been explained in the above section. It consist of bare $YBa_2Cu_3O_{7-\delta}$ wires, connected by a Au bar. Therefore, two patterning steps and etching are necessary, one to fabricate the $YBa_2Cu_3O_{7-\delta}$ wires out of a $YBa_2Cu_3O_{7-\delta}$ thin film, and one to create the Au bar connecting the wires.

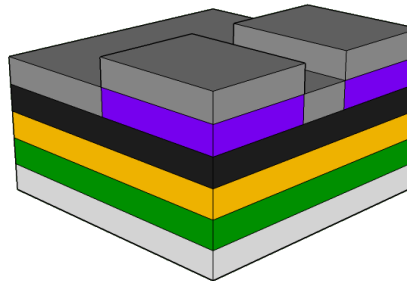
A detailed fabrication process final device layout process is given in table 6.1 below. Some details about the device layout changed over time, as discussed in section 6.5.1. In addition, some fabrication steps had to be optimised, as is detailed in section 6.5.2.

Table 6.1: A schematic overview of the sample fabrication process

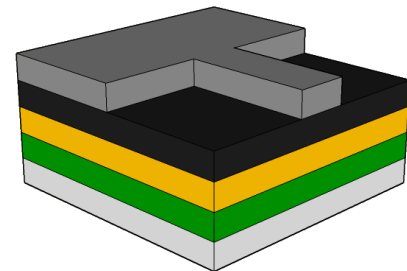
step 6: Electron-beam lithography to pattern the resist and resist development in hexylacetate



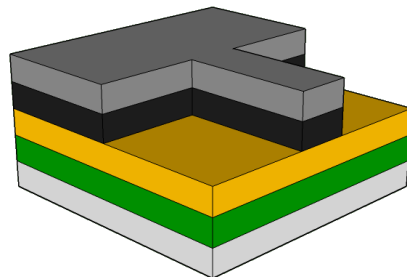
step 7: Deposition of 12nm thick Chromium layer on top of the developed resist



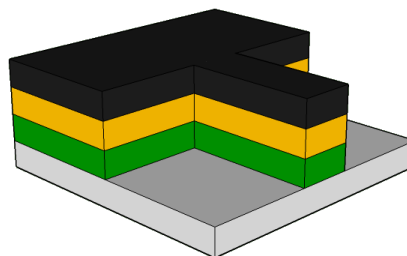
step 8: Liftoff of resist, transfer of ebeam pattern to chromium layer. The patterned Cr layer serves as a mask to protect the carbon layer underneath.



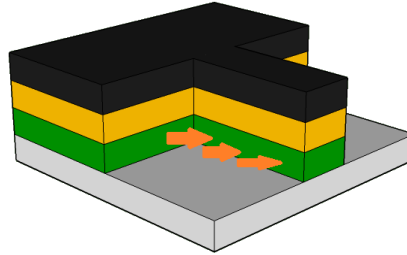
step 9: Etching of carbon layer by reactive oxygen plasma etch.



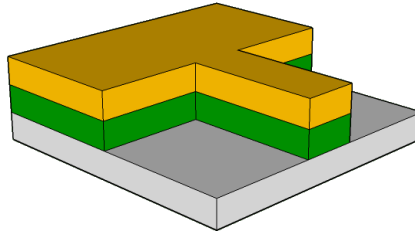
step 10: Etching of the $YBa_2Cu_3O_{7-\delta}$ -Au layer by Ar ion milling, this also removes the Cr layer on top of the carbon.



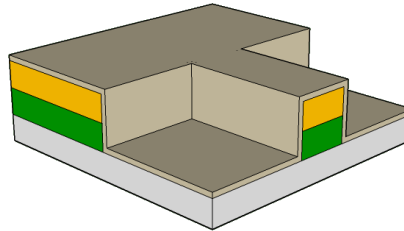
step 11: Ar ion milling of the side of the wires to create a tunnel barrier. Etching times and etch voltages were varied for different samples.



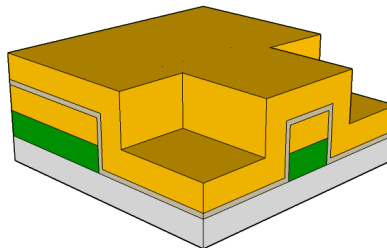
step 12: Removal of the carbon pattern by reactive oxygen plasma etch



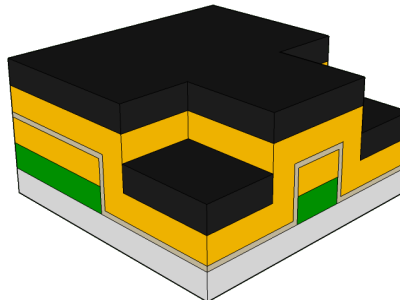
step 13: Deposition of thin Pt layer to ensure good adhesion of the subsequent layers to the sides of the $YBa_2Cu_3O_{7-\delta}$, by sputtering



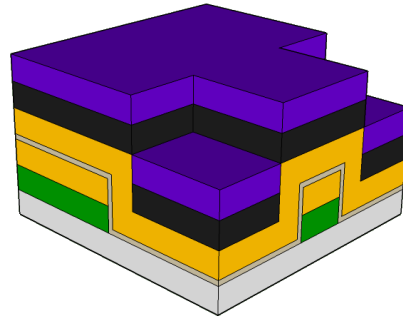
step 14: Deposition of 100nm thick Au layer on top of the $YBa_2Cu_3O_{7-\delta}$ by sputtering



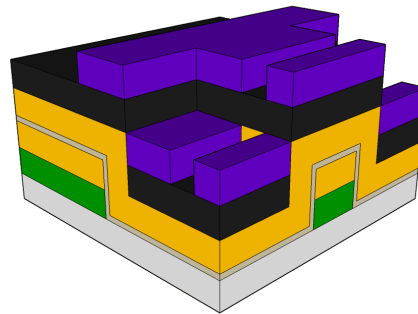
step 15: Deposition of 80nm thick carbon layer on top of Au by evaporation of pulsed laser deposition.



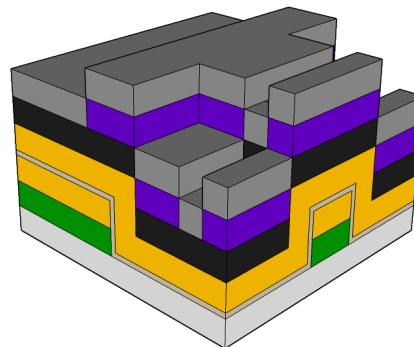
step 16: Resist spinning and baking on top of Carbon.



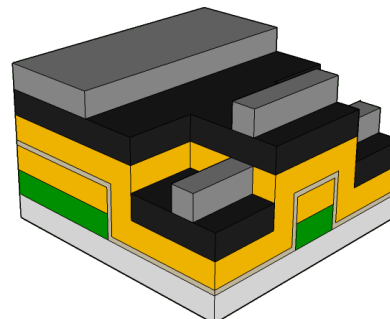
step 17: Electron-beam lithography to pattern the resist and resist development in hexylacetate.



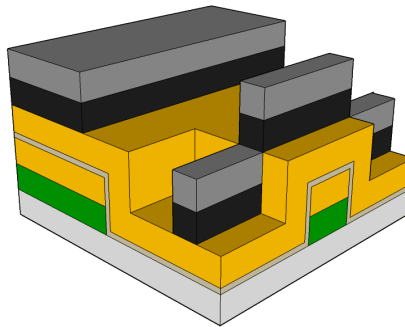
step 18: Deposition of 12nm thick chromium layer on top of the developed resist



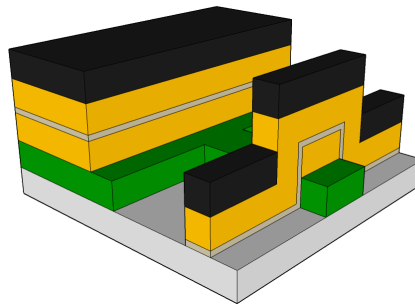
step 19: Liftoff of resist, transfer of ebeam pattern to chromium layer.



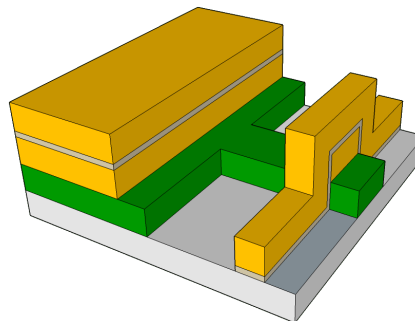
step 20: Etching of carbon layer by reactive oxygen plasma etch.



step 21: Etching of the Au layer on top of the MgO and the $YBa_2Cu_3O_{7-\delta}$ wires at 250V, this also removes the Cr.



step 22: Removal of the carbon pattern by reactive oxygen plasma etch



6.4 Ozonation treatment

The ozonation treatment is carried out in an O_2 rich environment at $150^\circ C$ for 2 hours. An UV light is shining upon the sample and creates ozone out of the oxygen. After two hours, the UV light is turned off and the sample is allowed to cool down slowly for two hours while oxygen rich gas is blown over the sample.

After ozone treatment, the sample is measured again as described above.

6.5 Evolution of the Device Layout and Fabrication Process

6.5.1 Evolution of Device Layout

The evolution of the layout of the very first samples fabricated to the final ones happened in two big steps. The basic layout of the device, 4 parallel $YBa_2Cu_3O_{7-\delta}$ nanowires connected by a gold bar, remained unchanged.

In the very first samples, the $YBa_2Cu_3O_{7-\delta}$ nanowires were completely covered with gold to protect them from the external environment, oxygen diffusing away and etching damage during the final etching step. In addition, the distance between the 4-point measurement electrodes and the gold bar was around $30\mu m$. In total, 5 working samples were fabricated and measured. The surface of them were treated with Ar ion milling with an etching voltage of 200V for 5 minutes, 250V for 5min (two samples), 250V for 10min and 250V for 15min respectively. In one of the samples treated with 250V for 5min, the $YBa_2Cu_3O_{7-\delta}$ nanowires were in direct contact with a thin Pt layer both on the sides and top, followed by a Au layer, instead of having only a Pt layer on the sides. The extracted contact resistivities, done as described in section 6.2, barely varied between the samples. This was a consequence of the gold coverage of the nanowires. As the entire device is covered by gold, the current could flow through the gold bar without having to redistribute into the $YBa_2Cu_3O_{7-\delta}$. As the contact resistance in these sample was high, it was also energetically unfavourable for the current to redistribute into the $YBa_2Cu_3O_{7-\delta}$ and then back into the gold bar, crossing the interface. As a result, the current did not cross the intended nano-sized Au- $YBa_2Cu_3O_{7-\delta}$ junction. An overview of the obtained contact resistivities of these samples is given in table 6.2.

Table 6.2: The obtained contact resistance for the first samples, where the $YBa_2Cu_3O_{7-\delta}$ nanowires were completely covered in gold

Sample treatment (etch voltage and time)	$\rho_c^{top} [Ohmcm^2]$	$\rho_c^{side} [Ohmcm^2]$
200V, 5min	7.59×10^8	7.42×10^8
250V, 5min	7.87×10^8	4.13×10^8
250V, 5min (Pt on top)	5.68×10^8	4.13×10^7
250V, 10min	8.26×10^8	1.33×10^7
250V, 15min	7.72×10^8	6.31×10^7

The next samples were fabricated with the same layout, but now the gold covering the $YBa_2Cu_3O_{7-\delta}$ nanowires was also etched away in the final etching step. The etching parameters were 200V for 10min and 250V for 10 min. The measured resistances were in the order of 10kOhm, but the data showed great variability, making an accurate analysis impossible. A possible explanation for the variability is that some of the $YBa_2Cu_3O_{7-\delta}$ nanowires were no longer superconducting and thus contributed also to the measured resistance. This is plausible, since the wires were very long ($\pm 30\mu m$), thus there was a greater chance for defects to be present or to be formed during the final gold etching step.

The final working devices consisted of 4 parallel $YBa_2Cu_3O_{7-\delta}$ nanowires, 1 μm long and not covered in gold, with wide electrodes on both sides. This allowed to check if each wire was still superconducting and to measure the critical current of the wire by a 4 points measurement. Part of the electrodes were also not covered in gold to make sure that all the current was flowing in the $YBa_2Cu_3O_{7-\delta}$ layer well before the beginning of the 4 point measurement and that it crossed the intended interface. A schematic representation of part of the device is given in figure 6.5

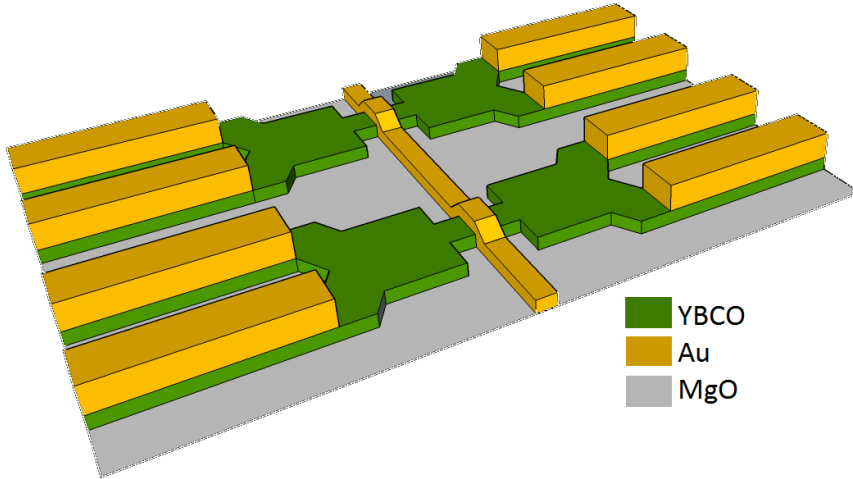


Figure 6.5: An illustration of the final device structure. The nano-wires are very short to preserve their superconductivity and are not covered by gold to force the current to flow in the $YBa_2Cu_3O_{7-\delta}$ layer and cross the intended interface.

6.5.2 Evolution of the fabrication process

The evolution of the fabrication process follows the evolution of the device layout in some manner.

For the first set of samples, the carbon hard mask was evaporated using pulsed laser deposition (PLD). The gold etching in step 21, table 6.1, was also rather aggressive since no gold on top of $YBa_2Cu_3O_{7-\delta}$ needed to be etched away. The two gold layers were also deposited by sputtering.

The fabrication of this first set of samples was very prone to failure due to bad adhesion of the second carbon layer to the underlying gold layer. During the second lift-off, step 19, the carbon layer would flake off, starting from the edges of the sample. This often caused that no carbon mask would be present on top of the bonding pads. As a result, they would be no longer covered with gold and had undergone some severe etching damage. The measurements from these samples were unreliable due to the deteriorated $YBa_2Cu_3O_{7-\delta}$ bonding pads and the bad contacts the wire bonding made with them. From the 11 fabricated samples, there were only 5 samples with good adhesion of the second carbon layer, which are mentioned and discussed above. Interestingly enough, this issue was only observed with the second carbon layer, never with the first. This might indicate that the patterned features of the gold layer are of influence on the adhesion of carbon. Extra cleaning of the gold layer, even with ozone plasma, did not remedy the issue. Starting from a lower laser energy of the PLD laser for the carbon deposition and gradually increasing it to its final value seemed to improve the adhesion. However, the carbon layer would still flake off sometimes. Evaporating a carbon layer on top of the gold, instead of depositing it with a pulsed laser deposition, fixed the issue completely. For the second and third set of samples, the greatest difficulty was the optimisation of

the etching of the gold layer on top of the $YBa_2Cu_3O_{7-\delta}$ nanowires away. Using the same etching voltage as for the previous sample proved to damage the $YBa_2Cu_3O_{7-\delta}$ nanowires too much and was too difficult to control precisely.

Etching with 250V seemed to offer a better control and damaged the $YBa_2Cu_3O_{7-\delta}$ less. However, the Cr layer on top of the carbon needs to be also etched away during this gold etching step in order to be able to remove the carbon mask in the subsequent step. This Cr layer could not be removed with 250V as etching voltage. To solve this issue, the thickness of the second gold layer was increase from 50nm to 100nm. This allowed to first etch the Cr on top of carbon away using 300V, while still having a thick enough gold layer to protect the underlying $YBa_2Cu_3O_{7-\delta}$. This left-over gold was then etched away using 250V.

The final change was to evaporate the gold layer on top of the $YBa_2Cu_3O_{7-\delta}$ instead of sputtering, as sputtering involves higher energy Au atoms which might break down the barrier.

6.6 Measurement set-up

The sample was glued with a low-temperature resistant glue to a chip carrier with 44 bonding pads. The fabricate device was connected to the chip carrier by wire bonding between the pads and the $YBa_2Cu_3O_{7-\delta}$ -Au electrodes, using a Au or AlSi wire. The chip carrier was then put into a 4K cryostat and cooled down to 4 Kelvin, by inserting the dip-stick in a LHe dewar, which stood inside an electromagnetic shielded room

The electronic measurement set-up is seen in figure 6.6. All digital components are outside the shielded room to prevent digital noise to affect the obtained data and there are low-noise filters between the components inside the shielded room and outside the room. Measurements are done by current-biasing the device by sending a voltage signal through a bias resistor, R_b , thus converting the voltage signal into a current signal. The voltage drop over the device is amplified by a voltage amplifier, while the current signal through the device is measured in an indirect way over a sample resistor, R_s , by a current amplifier. Both amplified voltage and current signals are then measured by 2 multimeters and recorded by the computer using a data acquisition card. The input voltage signal is generated by a function generator.

The following list details the electronics used in the measurements:

- 2 Stanford Research SR560 voltage amplifiers
- 2 HP 34401A multimeters
- 1 Fluke PM3380A oscilloscope
- 1 Agilent 33220A arbitrary function generator
- 1 National Instruments PCI-6052E data acquisition card.

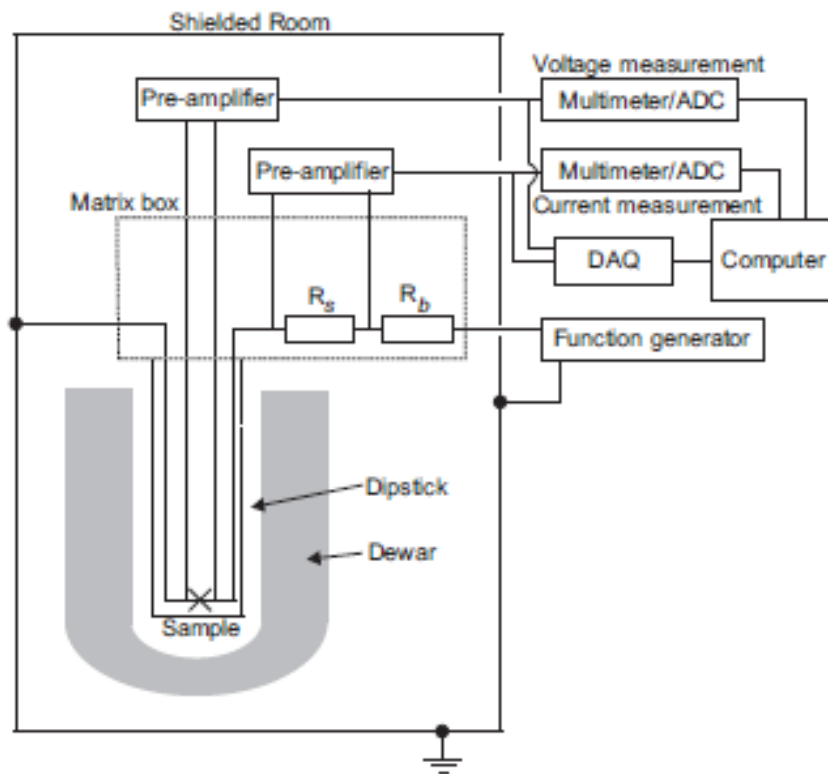


Figure 6.6: A schematic representation of the measurement set-up used to measure the samples. From [16]

7

Results and Discussion

7.1 Introduction

In this chapter the IV characteristics of $\text{Au}/\text{YBa}_2\text{Cu}_3\text{O}_{7-\delta}$ junctions fabricated with different etching procedures are analysed.

Before measuring the $\text{Au}/\text{YBa}_2\text{Cu}_3\text{O}_{7-\delta}$ contact resistance, the superconducting properties of the nanowires were characterized to assess the reliability of our nano-fabrication process. In the next step, the junctions are investigated by sending current from one superconducting nanowire through the gold bar to another. The obtained current-voltage characteristics of the $\text{Au}-\text{YBa}_2\text{Cu}_3\text{O}_{7-\delta}$ interfaces are then compared to the theoretical characteristics of NS and NIS junctions (see chapter 5) to help understanding the effect of the surface treatment on the interface. The contact resistivity of the side and the top is extracted from the measured resistance, as explained in chapter 6.

Each sample has been characterized twice, once as fabricated and a second time after ozone treatment. It is assumed that the ozone treatment replenishes the oxygen vacancies in damaged $\text{YBa}_2\text{Cu}_3\text{O}_{7-\delta}$ and helps to recover the superconducting state.

In total 6 samples were fabricated and measured. Their surface treatment was as follows: no treatment (ex situ gold on top), 200V for 2min, 200V for 5min, 200V for 10min, 250V for 5min and 300V for 5min. In the last two samples there was a problem with the alignment of the gold bar, thus only the critical current of the nanowires could be measured. Each sample consisted of 4 devices as described in section 6.2. They will be referred to as the 100nm, 200nm, 300nm, 400nm and 500nm device, after the width of the $\text{YBa}_2\text{Cu}_3\text{O}_{7-\delta}$ wires they consist of.

7.2 The critical current density of the $YBa_2Cu_3O_{7-\delta}$ nanowires

The critical current of the nanowires was measured using a 4-point measurement set-up. The critical current I_c was extracted as the largest value of the current for which no voltage drop was measured over the nanowire. By dividing over the estimated cross-section of the wire (50nm x width of nanowire), the critical current density J_c was obtained. Figure 7.1 shows the average J_c for the different widths of the wire before and after ozonation for all the six fabricated samples. Unfortunately not all measured wires were superconducting, so a complete comparison is not possible. However, it can be clearly seen that the wires that did not undergo any surface etching before gold deposition have a much higher J_c than all the rest.

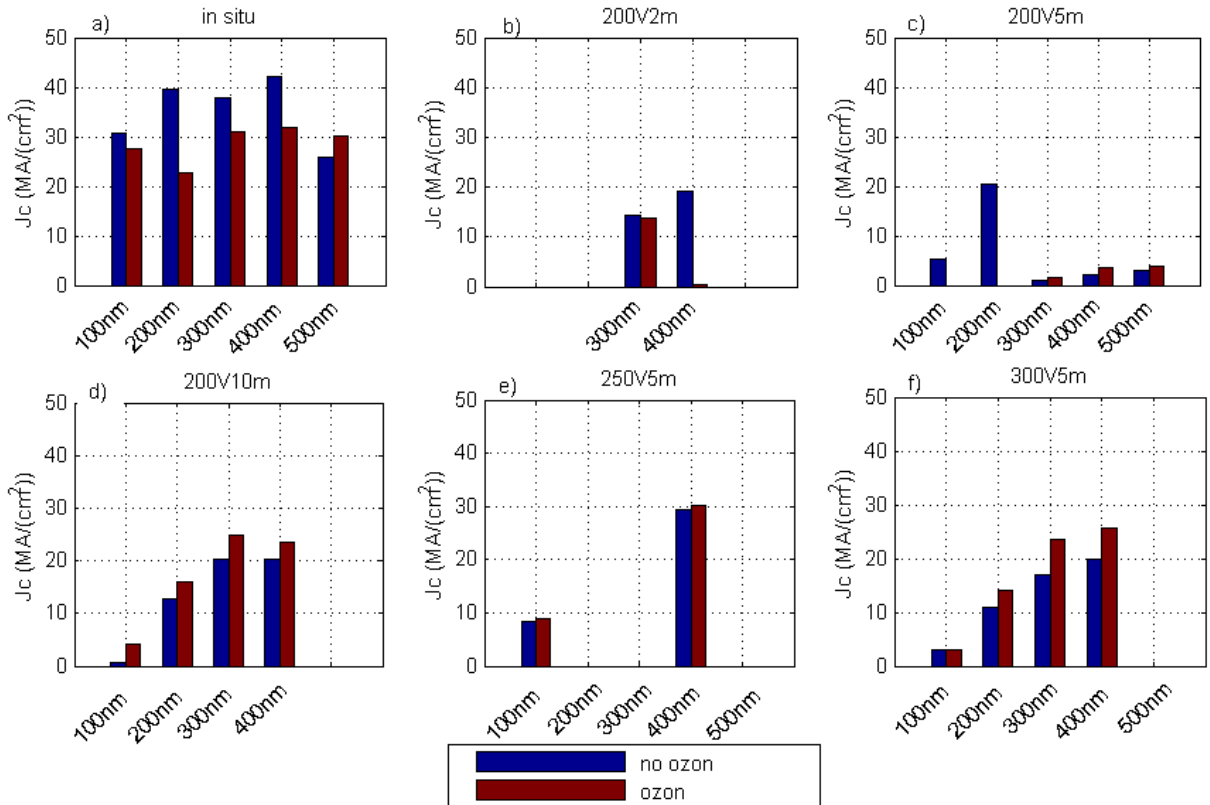


Figure 7.1: The average J_c of the nanowires with different widths and of the different samples, before and after ozonation. Etching parameters: a) no surface etching, b) 200V for 2 min, c) 200V for 5min, d) 200V for 10min, e) 250V for 5min, f) 300V for 5min.

The critical current density decreases as the width of the wire decreases, as can be seen particularly for figure 7.1d), e) and f). This is within expectations, since small wires have a higher surface to volume ratio and the surface undergoes etching damage during

fabrication. The spread in values of J_c for different etching procedures cannot be directly ascribed to the surface/side treatment. It might be due to the removal of Au from part of the nanowires in the last fabrication step. Slight etching into the $YBa_2Cu_3O_{7-\delta}$ nanowire after the complete removal of Au has been shown to strongly affect the critical current density of the nanostructure [28]. However, the clear decrease in the average J_c between the no treatment sample and some of the other samples (see figure 7.1a, d) and f)) might indicate that the surface treatment also affects the J_c . By treating the wires with ozone, the J_c increases in almost all cases, except for the no treatment and 200V for 2min sample. This increase in J_c after ozonation is most probably due to a change in the doping of $YBa_2Cu_3O_{7-\delta}$ as ozonation might replenish the oxygen vacancies in the nanowires. Since the no treatment sample did not undergo mild etching, increasing its oxygen content might move it further away from the optimal doping point, which might explain the observed decrease in J_c .

7.3 IV characteristics of the no treatment sample before and after ozonation

7.3.1 IVC before ozonation

Some typical IV curves of $2Au/YBa_2Cu_3O_{7-\delta}$ interfaces (each consisting of one top interface and two side interfaces) in series with a Au bar are shown in figure 7.2. A clear non-linearity is visible for the 100nm, 200nm and 300nm device.

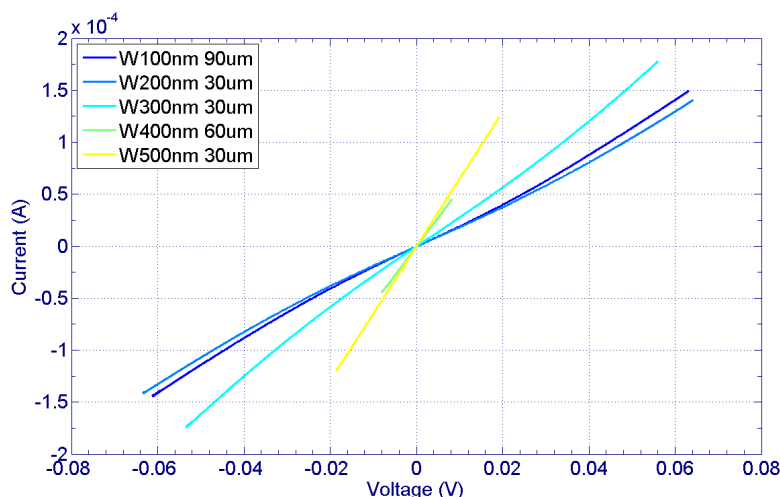


Figure 7.2: Some typical IV curves of the different devices of the no treatment sample.

The obtained conductance-voltage curves can be seen in figures 7.3a, 7.4a, 7.5a, 7.6a and 7.7a. The legend indicates the length of gold bar between the two probed $YBa_2Cu_3O_{7-\delta}/Au$ interfaces. The position of the $YBa_2Cu_3O_{7-\delta}$ gap, which is indicated

by black arrows, is observable in the 100nm device.

The 400nm and 500nm conductance curves are linear. A common distinct feature of the conductance-voltage curves of the 100, 200 and 300nm devices is the V-shaped background. In addition, the curves are also not symmetric around zero bias. The 200nm devices shows a flat region around zero bias with possible a small ZBCP present in one curve.

It should be noted that the voltage range was small, and in hindsight should have been larger to get a clearer picture.

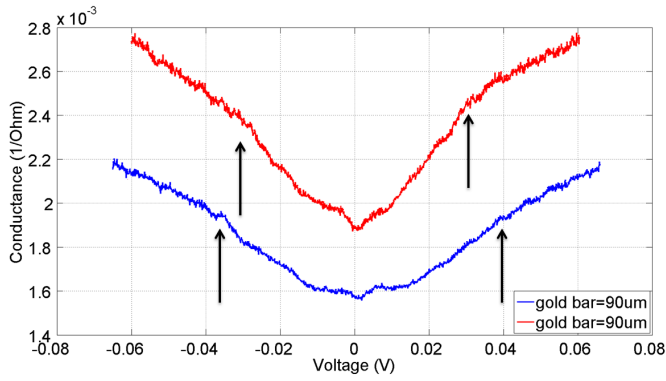
7.3.2 IVC after Ozonation

Similar to before the ozonation, the IV curves were non-linear. The biggest change compared to before the ozone treatment is for the 400nm and 500nm which now show non-linear behaviour. The obtained conductance curves can be seen in figures 7.3b, 7.4b, 7.5b, 7.6b and 7.7b.

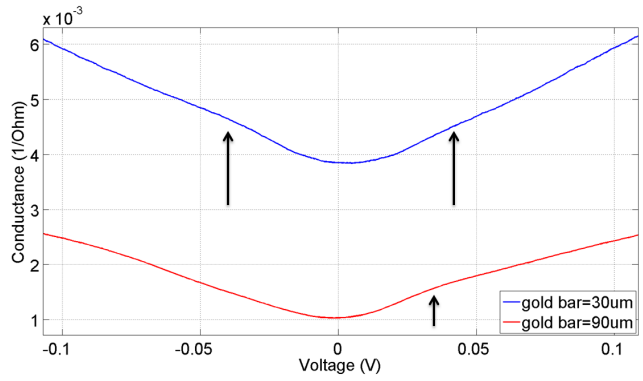
Where possible, the same devices were compared before and after ozonation. Sometimes this was not possible because the same wires were no longer superconducting after ozonation.

Gap features are still visible in the 100nm device, and are especially pronounced in the 200nm device, which shows typical tunnel characteristics. The conductance curves of the 400nm and 500nm devices show a inflection point around 40-50mV, which can be attributed to the presence of the $YBa_2Cu_3O_{7-\delta}$ gap. The presence of the inflection point is illustrated for the 400nm device. The 300nm device curves do not show an inflection point and look parabolic. However, in this case the voltage range was too narrow to detect a change in slope due to possible gap features.

7.3. IV CHARACTERISTICS OF THE NO TREATMENT SAMPLE BEFORE AND AFTER OZONATION 55

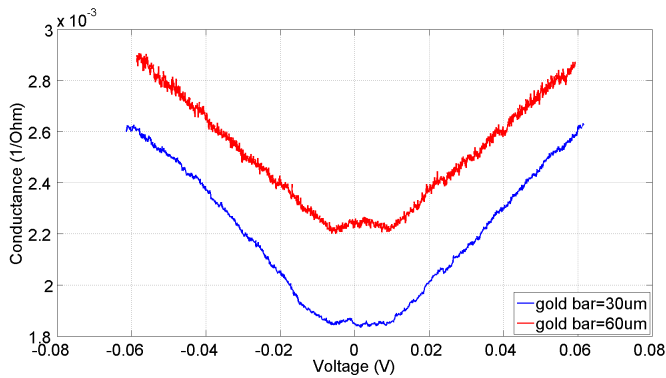


(a) before ozone treatment

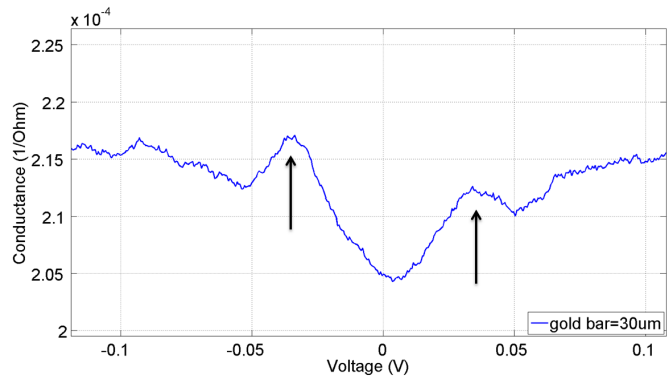


(b) after ozone treatment

Figure 7.3: A comparison of the conductance curves of the 100nm no treatment device before and after ozonation

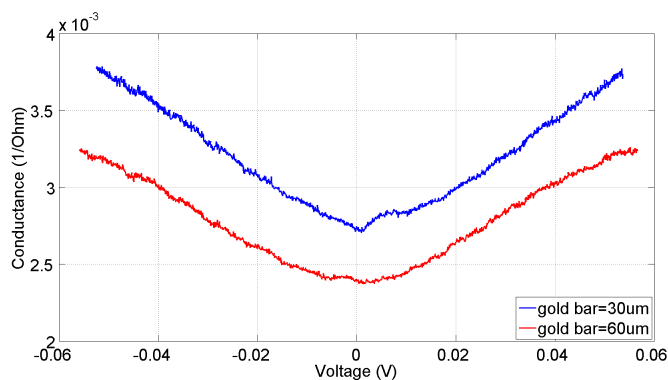


(a) before ozone treatment

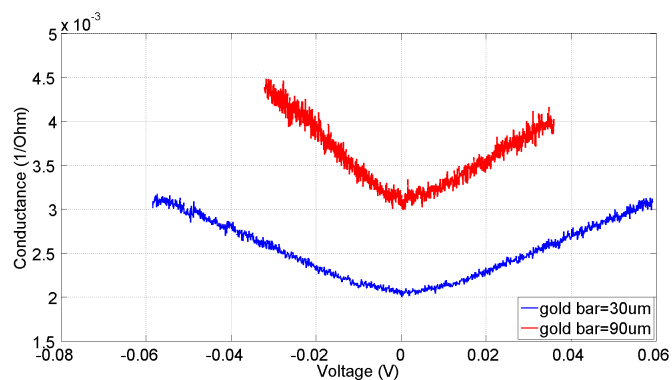


(b) after ozone treatment

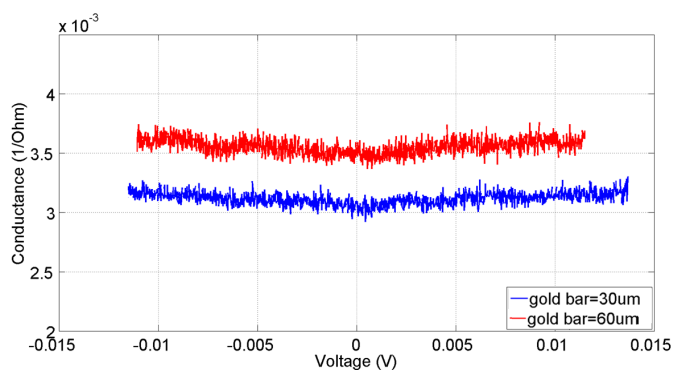
Figure 7.4: A comparison of the conductance curves of the 200nm no treatment device before and after ozonation



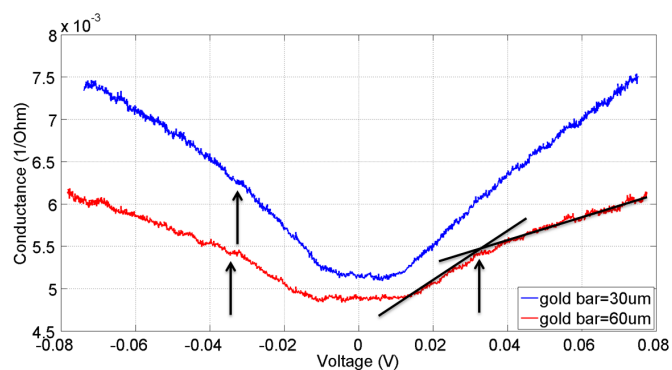
(a) before ozone treatment



(b) after ozone treatment

Figure 7.5: A comparison of the conductance curves of the 300nm no treatment device before and after ozonation

(a) before ozone treatment



(b) after ozone treatment

Figure 7.6: A comparison of the conductance curves of the 400nm no treatment device before and after ozonation. The position of the inflection point is indicated.

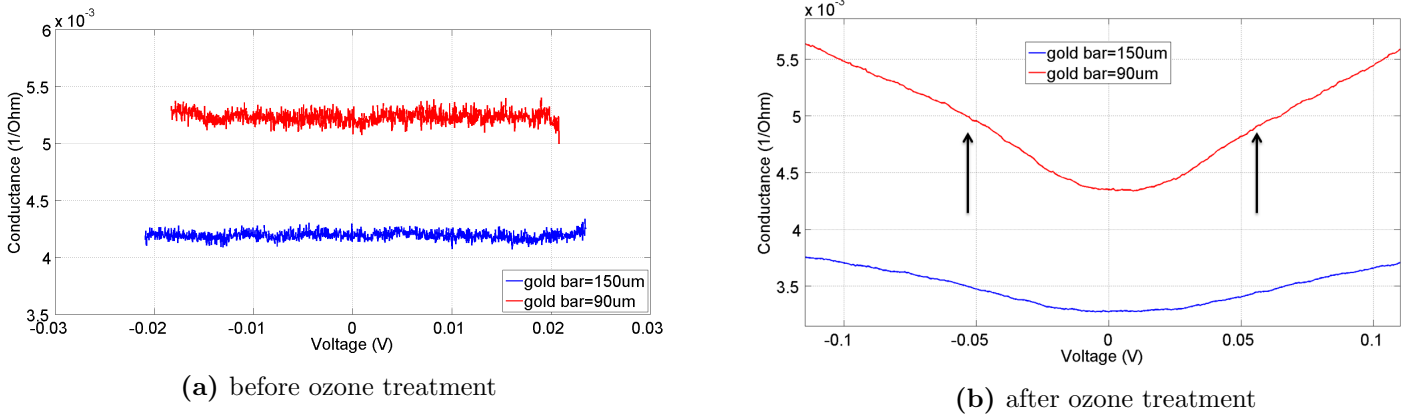


Figure 7.7: A comparison of the conductance curves of the 500nm no treatment device before and after ozonation

7.3.3 The contact resistance before and after ozonation for no treatment sample

The contact resistance was extracted as explained in section 6.2. The total measured resistance is equal to $R_{tot} = R_{c1} + R_{Au} + R_{c2} = r_{Au}l + R_{c1} + R_{c2}$, and depends linearly on the length of the gold bar connecting the two $YBa_2Cu_3O_{7-\delta}$ nanowires. In addition the contact conductance depends linearly on the area of the top contact A between the Au bar and $YBa_2Cu_3O_{7-\delta}$ nanowire: $G_c^{tot} = 1/(R_c) = 2G_c^{side} + G_c^{top} = 2G_c^{side} + g_c^{top}A$. The width of the Au bar connecting the two nanowires was 500nm for all devices, thus $A = 500nm \times width_{nanowire}$.

The conductance curve of our devices are bias dependent even at voltages higher than 2Δ . For this reason, it is important to choose a good voltage criteria for extracting the resistance of the device. Since typical SET experiments are performed at source-drain voltages smaller than few millivolt, the resistance value was taken at 5mV. Unfortunately, the data points were too scattered to reliably extract the contact resistance. This can be easily seen from figure 7.8, where the slopes of the linear fits differ greatly between different devices, while they should all be equal and corresponding to the resistivity of the gold bar per unit length ($\Omega/(\mu m)$). Thus the value of the contact resistances of the Au- $YBa_2Cu_3O_{7-\delta}$ junction $R_{c1} + R_{c2}$ can not be reliably extracted from the intercept of the linear fit. This might be due to great variability of the contact resistance between different $YBa_2Cu_3O_{7-\delta}$ nanowires of the same device.

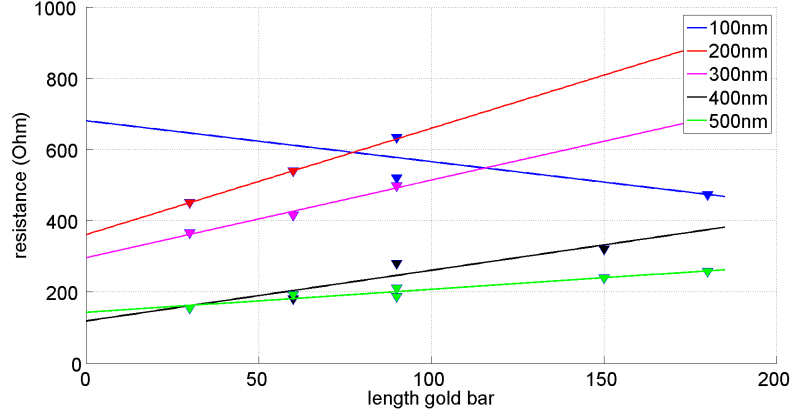


Figure 7.8: The resistance extracted at 5mV of the different devices as a function of the length of the gold bar connecting the two $YBa_2Cu_3O_{7-\delta}$ nanowires.

The intercept of the linear fits does not correspond to the contact resistance, however, $R_{c_1} + R_{c_2}$ for each device can still be estimated as follows. The estimated resistance of the gold bar was subtracted from each datapoint of figure 7.8. By dividing these values by two, the average contact resistance, $R_{c_{av}}$ of the $YBa_2Cu_3O_{7-\delta}$ nanowire-Au junction is obtained for each device.

The corresponding conductance values were calculated and plotted as a function of the contact top area A in figure 7.10.

The dependence of the average contact conductance on the top contact area of the $YBa_2Cu_3O_{7-\delta}$ -nanowire before can be seen in figure 7.10.

Due to the low statistics only the lower bound of the top contact resistivity is estimated using the first three data sets from $0.5 \cdot 10^5 \text{ nm}^2$ to $1.5 \cdot 10^5 \text{ nm}^2$. This is done by taking the maximum slope of a linear curve passing through the points. The slope of the contact conductance as a function of the area is proportional to the inverse of the top contact resistivity (see section 6.2). From the intercept of the linear curve the side contact resistivity can be determined. It is worth noting that the data sets corresponding to the 400 nm and 500 nm device are not included in the analysis, since they depart too much from a linear behaviour. The values we get for the top and side resistivities are $5.0 \times 10^{-7} \text{ Ohmcm}^2$ and $1,8 \times 10^{-7} \text{ Ohmcm}^2$.

A typical SET layout would consist of a $YBa_2Cu_3O_{7-\delta}$ rectangular island, 100 nm high and of variable width, as illustrated in figure 7.9. The gold electrodes would cover the first 100 nm of the $YBa_2Cu_3O_{7-\delta}$ island. For this layout, the obtained contact resistivity values would correspond to a total contact resistance of 535 Ohm if the width of the $YBa_2Cu_3O_{7-\delta}$ island was 100 nm (thus the top contact equals 100 nm x 100 nm), which is much smaller than the quantum resistance, R_Q .

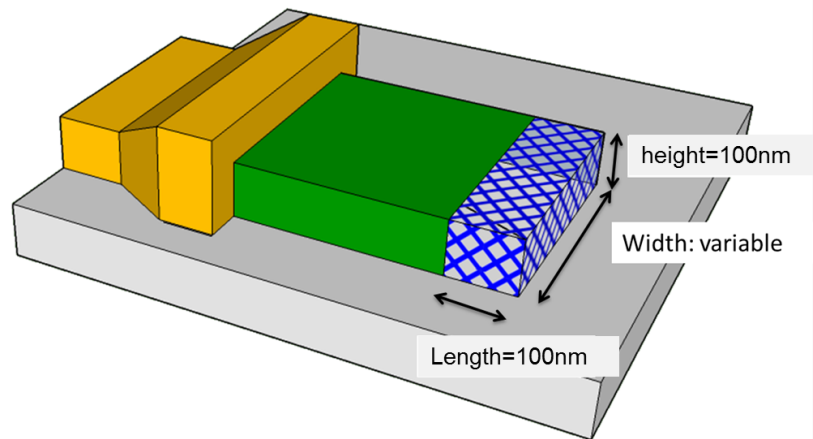


Figure 7.9: A schematic representation of a proposed SET layout. The gold electrode is shown on the left side, while the marked area on the right of the $YBa_2Cu_3O_{7-\delta}$ island shows the contact area between the gold electrode and the $YBa_2Cu_3O_{7-\delta}$.

After ozonation, the resistances for the different lengths of the gold bar were extracted in the same way. The same problem arose when trying to plot them as a function of the length of the gold bar. Therefore we proceeded in the same way as before ozonation. The resulting plot of the estimated average contact resistance for each device as a function of the top contact area can be seen in figure 7.11. The data points are now too scattered to extract reliable values for the top and side resistivities. All attempts to estimate the slope of a linear interpolation give values of the top resistivities close to the ones before ozonation. This indicates that the ozone treatment does not strongly affect the superconducting $YBa_2Cu_3O_{7-\delta}/Au$ interface.

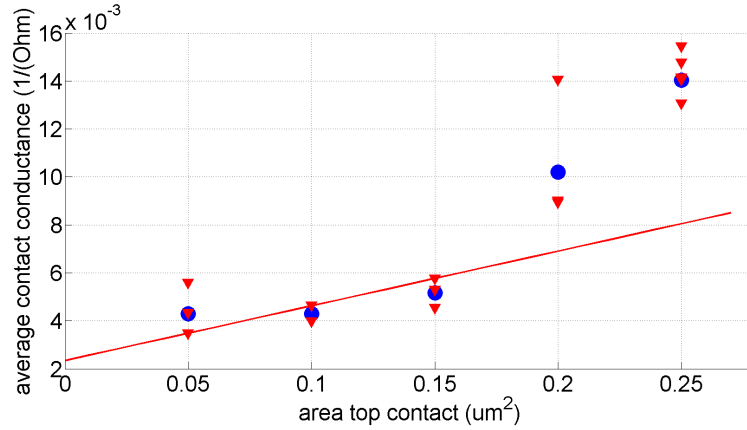


Figure 7.10: The average contact conductance as a function of the top area of the wires before ozonation. The apparent change between the 300nm device and 400nm device is clearly visible. The red triangles are the G_c values for each device, the blue dots indicate the average G_c of them.

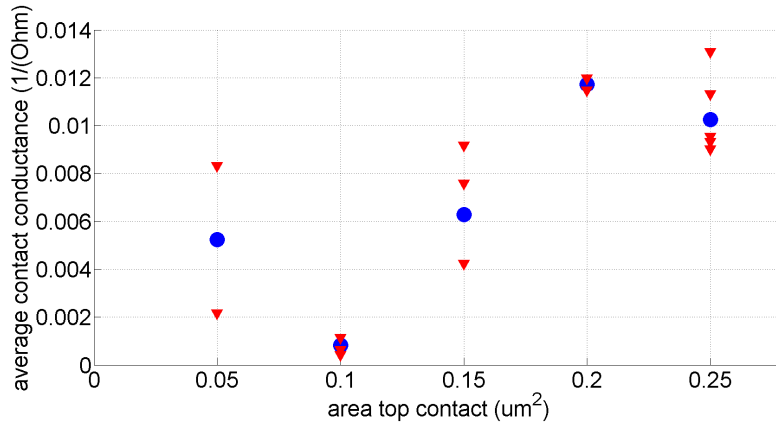


Figure 7.11: The average contact conductance as a function of the top area of the wires after ozonation. The red triangles are the G_c values for each device, the blue dots indicate the average G_c of them.

7.3.4 Interpretation of the results: the non treated interface and effect of ozonation

All non-linear conductance curves shown above have a linear background and most are asymmetric around zero bias. A linear background is a common feature of a lot of $YBa_2Cu_3O_{7-\delta}$ tunnel junctions and is commonly attributed to inelastic scattering [23]. The asymmetry of the conductance curves on the other hand reflects the asymmetry of the potential barrier. The gap features at approximately $\approx 2\Delta$, corresponding to the two $\text{Au-YBa}_2\text{Cu}_3\text{O}_{7-\delta}$ interfaces in series, is only clearly seen in the 100nm device before ozonation (see figure 7.3a). For larger area device ($>200\text{nm}$), the absence of a gap

feature might be related to a normal $YBa_2Cu_3O_{7-\delta}$ layer in series with the Au barrier interface, which dominates the transport through the interface, see figure 7.12 and is discussed in section 5.3. This size dependence of the presence of the gap feature points to the existence of normal $YBa_2Cu_3O_{7-\delta}$ regions of the order of $100 \times 500 \text{ nm}^2$. This would explain the linear IV characteristics for the 400nm and 500nm devices, where transport through the normal $YBa_2Cu_3O_{7-\delta}$ dominates.

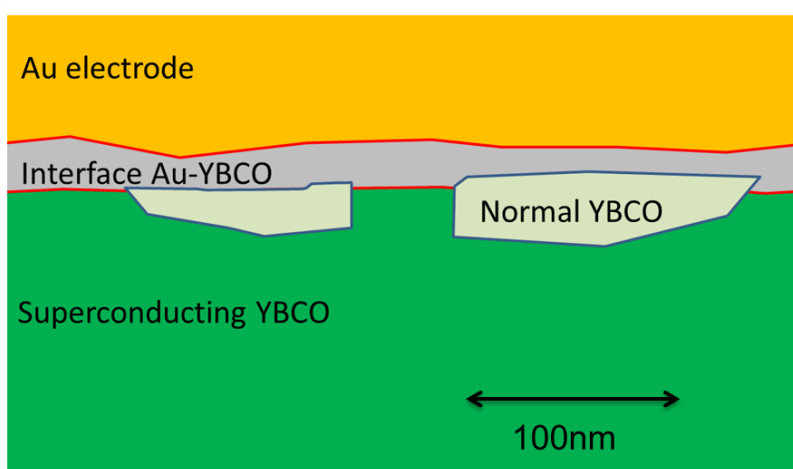


Figure 7.12: An illustration of the normal regions regions possible present at the interface

In this scenario, the normal $YBa_2Cu_3O_{7-\delta}$ -Au interface has to be much more transparent than the superconducting $YBa_2Cu_3O_{7-\delta}$ -Au interface. Moreover the contribution of the normal region has to dominate the value of the total resistance. However, only microscopic studies can confirm the validity of these assumptions. After ozonation, the gap structure becomes visible again in the 200nm device (see figure 7.4b), 400nm device (figure 7.6b) and 500nm device (figure 7.7b). Most probably, the ozone treatment restores the superconducting state in the normal $YBa_2Cu_3O_{7-\delta}$ regions. The fact that the total conductance remains unaffected (within a factor of two, see figure 7.10 and 7.11) might be justified by the simultaneous disappearance of the normal $YBa_2Cu_3O_{7-\delta}$ /Au interfaces and increase of the interface resistance of the newly recovered superconducting $YBa_2Cu_3O_{7-\delta}$ -Au interfaces. The obtained conductance curves also show little resemblance to the ones theoretically predicted by [8] and [38]. However, this might be due to the linear background that is superimposed on the other typical conductance features. As such, some of the conductance curves can be explained by assuming that around zero bias, inside the gap region, the predicted conductance features are observed, while for slightly higher bias, the linear background masks these features. It is useful to recollect the shape of the conductance curves for different barrier strengths Z and orientation angles α and the difference between tunnelling in the a-b plane and c-axis direction, as

is illustrated in figures 5.6 and 5.7.

The flat region around zero bias observed in the 200nm device before ozonation and 400nm and 500nm after ozonation might correspond to high barrier transparency as the Andreev reflection coefficient is flat inside the gap for high transparencies. For higher voltages the background dominates and the drop of A outside the barrier is masked.

To conclude, the no treatment Au/ $YBa_2Cu_3O_{7-\delta}$ interface has a too low contact resistance to fabricate a SET. Patches of normal $YBa_2Cu_3O_{7-\delta}$ are present and mask out the predicted tunnel and Andreev reflection features for large area devices (>200 nm). Ozonation restores the superconductivity in these normal patches, causing gap features to appear.

7.4 The IV characteristics of the 200V 5min sample

Of the 200V for 5min sample, only the 300nm, 400nm and 500nm device were working, as the wires in the other devices were not superconducting.

7.4.1 IVC before ozonation

Typical IV curves for the different devices are shown in figure 7.13. They are all clearly non-linear. The conductance spectra all showed a parabolic or linear background and are asymmetric around zero voltage.

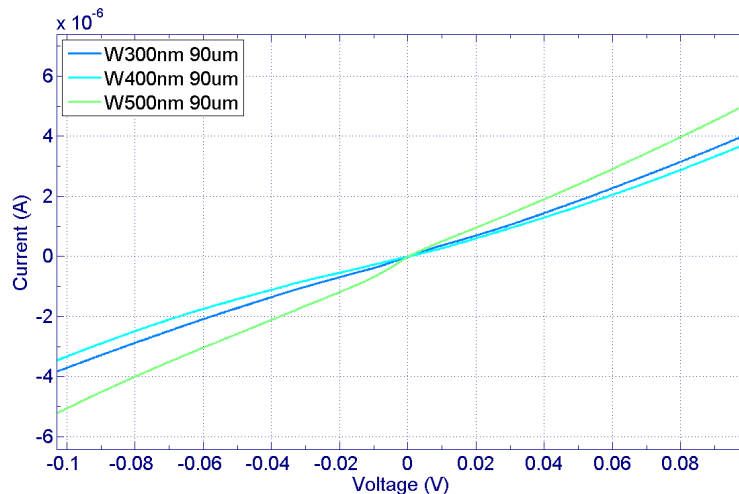


Figure 7.13: Some typical IV curves of the different devices of the 200V5m sample.

The conductance curves of the 300nm device show a clear gap structure around 40mV and a forked peak inside the gap which is very pronounced for one measurement and less for the other, see figure 7.14a.

The 400nm device showed a linear, V-shaped background with a change in the slope above the gap and a small ZBCA structures in the middle (figure 7.15a).

The 500nm device showed a linear or parabolic background with a very pronounced and sharp ZBCP (figure 7.16a).

7.4.2 IV and conductance curves after ozonation

Both the IV and conductance curves maintain their non-linear behaviour. The linear background is still present in the conductance curves, as well as the asymmetry.

It was only possible to measure one configuration of the 300nm device. A clear gap structure is visible, with no ZBCA.

The shape of the conductance curves of the 400nm device did not change much after ozonation. The gap structure is still clearly visible and for one curve a ZBCP appeared. The very pronounced ZBCP of the 500nm device before ozonation increased in some cases and was reduced in other cases.

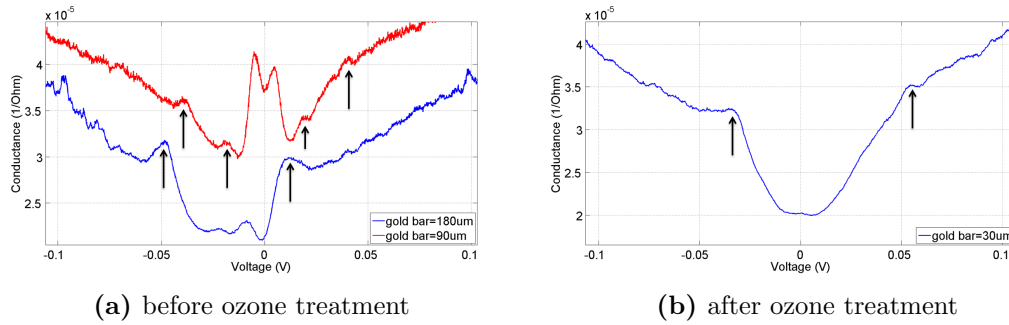


Figure 7.14: A comparison of the conductance curves of the 300nm 200V 5m device before and after ozonation

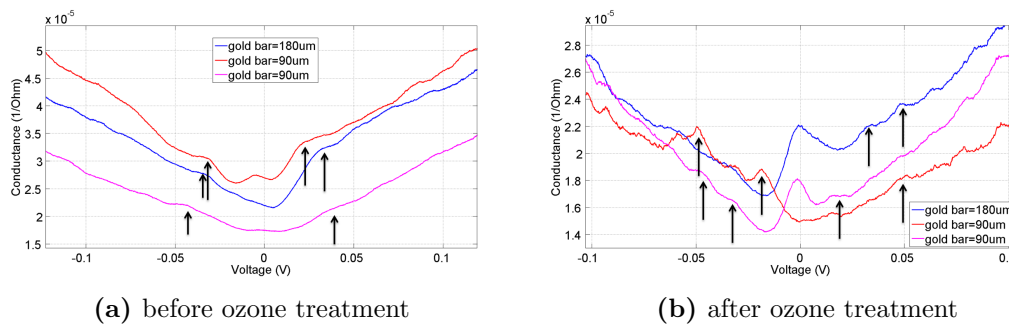


Figure 7.15: A comparison of the conductance curves of the 400nm 200V 5m device before and after ozonation

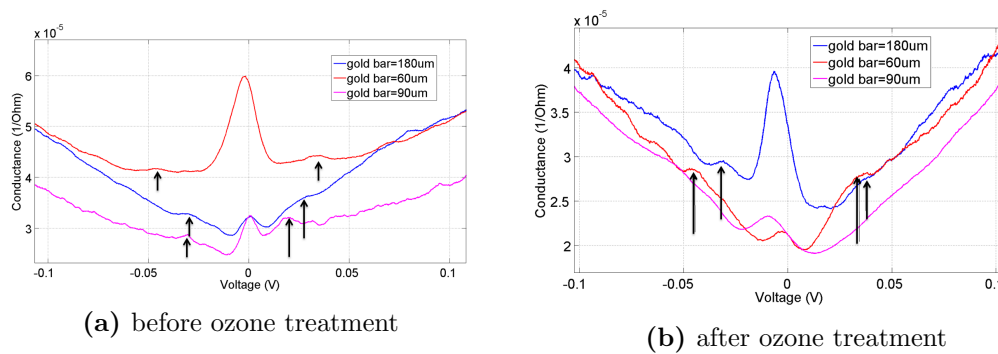


Figure 7.16: A comparison of the conductance curves of the 500nm 200V 5m device before and after ozonation

7.4.3 Extracting the contact resistance

We attempted to extract the contact resistance following the same procedure as for the no treatment sample. The same problems were encountered and the same solutions were used. The resulting contact conductance plots as a function of the top contact area of the wires can be seen in figure 7.17. The extracted contact resistivity after ozonation for the 200V 5 min device was $1,67 \times 10^{-4} \text{Ohmcm}^{-2}$ for the top and $1,7 \times 10^{-5} \text{Ohmcm}^{-2}$ for the side. The contact resistivity before ozonation could not be extracted, as there data was very scattered.

For a typical SET device layout, as shown if figure 7.9, with the height of the island 50nm the total contact resistance would be 55kOhm if the top contact area of the $YBa_2Cu_3O_{7-\delta}$ island with gold was 100nmx100nm and 33kOhm if the top contact area was 300nmx100nm. Both values are much higher than the quantum resistance, R_Q , thus fulfilling on of the working requirements to have a functional SET.

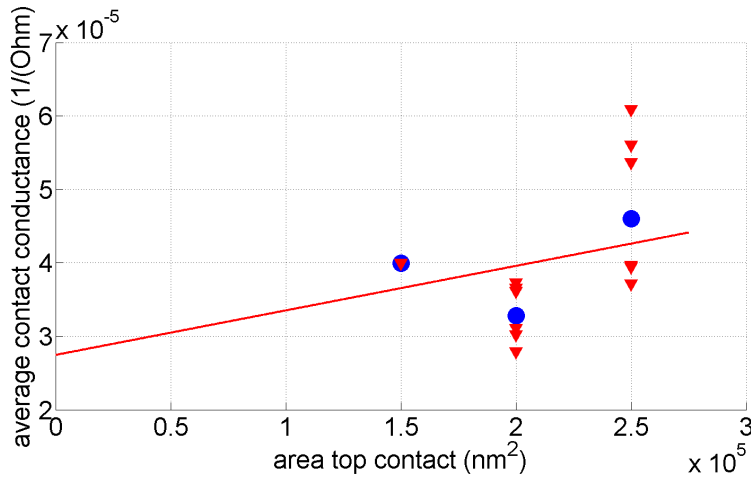


Figure 7.17: The average contact conductance as a function of the top area of the wires after ozonation for the 200V for 5m sample. The red triangles are the G_c values for each device, the blue dots indicate the average G_c of them.

7.4.4 Interpretation of the results: the 200V 5min interface and effect of ozonation

An explanation for the observed linear background and asymmetric conductance curves is already given in section 7.3.4 and might also be valid here.

The 300 nm devices before ozonation show a splitted peak around zero bias (see figure 7.14a which could be due to the presence of a normal $YBa_2Cu_3O_{7-\delta}$ layer at the interface with Au. Chiara et al. [11] derived a similar shape for a non-homogeneous superconductor modelled with a N'S' bilayer. Another possible explanation is the presence of a subdominant order parameter, which induces a splitted ZBCP, as shown by Deutscher et al [9][13].

According to Deutscher, the peak should become more pronounced in over-doped $YBa_2Cu_3O_{7-\delta}$, thus after ozonation. On the contrary, the disappearance of the peak after ozonation is in line with the expectations of the NIN'S' assumption. The superconductivity in N' is restored by the ozonation treatment and thus the splitted peak, caused by the N' layer at the interface disappears. Since the same configuration could not be measured after ozonation, the presence of this normal layer or the increase of the splitted peak could not be confirmed. The ZBCP in the 500nm device could be due to Andreev reflection at the interface. However, this would not explain their disappearance after ozonation for the red curve (see figure 7.16b) or the increase of ZBCP of the blue curve. ZBCP are also observed in the presence of the normal layer at the interface. In this scenario, the decrease after ozonation could be attributed to the disappearance of the normal layer, while the increase in the other curve to a reduction of the normal layer $YBa_2Cu_3O_{7-\delta}$ thickness.

Since the presence of a weakly coupled N'S' bilayer at the interface can explain the observed characteristics, this explanation seems the most likely. Similar arguments apply for the 400nm devices (see figure 7.15b). To conclude, after etching the surface of the $YBa_2Cu_3O_{7-\delta}$ nanowires with 200V for 5min, an inhomogeneous normal $YBa_2Cu_3O_{7-\delta}$ layer is formed below the interface. In this normal layer the superconductivity is partially / totally restored after ozonation. Ozonation might also decrease the transparency of the interface. Compared to the no treatment sample, the transparency of the interface is lower, causing a lower overall conductance and higher estimated contact resistivity

7.5 The IV characteristics of the 250V for 5 minutes device

The resistance of this sample was too high to be measured with our measurement set-up, even though the $YBa_2Cu_3O_{7-\delta}$ wires were superconducting. This indicates very high contact resistances were achieved, comparable with the input impedance of the amplifiers, of the order of 1 M Ω .

7.6 Follow-up Research

Suitable tunnel barriers have been fabricated and the fabrication of the SET can now be attempted. However, some questions remain about the nature of the interface. Some proposals for future work to increase our understanding of the Au/ $YBa_2Cu_3O_{7-\delta}$ interface and the effect of ozonation is outlined below.

The effect of ozonation could first be studied on bare films of different initial doping. Comparing the T_c before and after ozone treatment would give a clear indication if the doping of the film is affected. If the T_c barely varies, ozonation might only affect the surface layer and not the bulk. In addition, X-ray spectroscopy can also be used to see if the ozone treatment replenishes the oxygen vacancies and affects the structure of $YBa_2Cu_3O_{7-\delta}$.

The presence of normal layers can be studied by different ozone treatments and their

effect on the interface properties of $\text{Au}/\text{YBa}_2\text{Cu}_3\text{O}_{7-\delta}$. For shorter durations of the ozone treatment, the interface properties after ozonation might be different since the normal layer thickness is reduced less.

The effect of etching and ozonation on the $\text{YBa}_2\text{Cu}_3\text{O}_{7-\delta}$ surface can also be studied on bare films. After etching with 200V for 5 minutes, one can investigate the oxygen depletion of the surface similar to Suzuki et al. [36] by X-ray photoemission spectroscopy (XPS). Multiple cycles of etching the surface away followed directly by XPS measurements, should result in the depth profile of the oxygen content in $\text{YBa}_2\text{Cu}_3\text{O}_{7-\delta}$. This can also be an indication of the presence of the depth profile.

Lastly, more samples need to be measured to have better statistics and a more accurate value of the side and top contact resistivities.

7.7 Conclusion

The effect of multiple etching voltages and times on the $\text{Au}-\text{YBa}_2\text{Cu}_3\text{O}_{7-\delta}$ interface was examined at the nanoscale. Etching clearly increases the barrier strength and contact resistance, as well as damaging the superconducting state. In addition, conductance features are observed which can be attributed to an inhomogeneous normal $\text{YBa}_2\text{Cu}_3\text{O}_{7-\delta}$ layer at the interface. Ozonation seems to restore the normal $\text{YBa}_2\text{Cu}_3\text{O}_{7-\delta}$ to the superconducting state by replenishing created oxygen vacancies in $\text{YBa}_2\text{Cu}_3\text{O}_{7-\delta}$ by the surface treatment.

To conclude, we have engineered tunnel barriers between $\text{YBa}_2\text{Cu}_3\text{O}_{7-\delta}$ and Au that can be used for fabricating a SET by mild ion etching of the $\text{YBa}_2\text{Cu}_3\text{O}_{7-\delta}$ surface. It is a valid approach to fabricate SETs, provided that the superconducting state on the island is not destroyed by the etching. To ensure this, a big island size is advisable in addition to ozonation treatment.

Bibliography

- [1] A. F. Andreev. The thermal conductivity of the intermediate state of superconductors. *Soviet Physics JETP-USSR*, 19(5):1228–1231, 1964.
- [2] G. B. Arnold, J. Zasadzinski, and E. L. Wolf. A resolution of the controversy on tunneling in Nb. *Physics Letters A*, 69(2):136–138, 1978.
- [3] A. V. Balatsky. Spontaneous time reversal and parity breaking in a $d_{x(2)-y(2)}$ -wave superconductor with magnetic impurities. *Physical Review Letters*, 80(9):1972–1975, 1998.
- [4] J. Bardeen, L. N. Cooper, and J. R. Schrieffer. Theory of superconductivity. *Physical Review*, 108(5):1175–1204, 1957.
- [5] K. Bechgaard, K. Carneiro, M. Olsen, F. Rasmussen, and C. Jacobsen. Zero-pressure organic superconductor. *Physical Review Letters*, 46(13):852–855, 1981.
- [6] J. G. Bednorz and K. A. Müller. Possible high-T_c superconductivity in the BaLaCuO system. *Zeitschrift Für Physik B-Condensed Matter*, 64(2):189–193, 1986.
- [7] A. S. Bhalla, R. Y. Guo, and R. Roy. The perovskite structure - a review of its role in ceramic science and technology. *Materials Research Innovations*, 4(1):3–26, 2000.
- [8] G. E. Blonder, M. Tinkham, and T. M. Klapwijk. Transition from metallic to tunneling regimes in superconducting micor-constrictions -excess current, charge imbalance, and super-current conversion. *Physical Review B*, 25(7):4515–4532, 1982.
- [9] H. Castro, G. Leibovitch, R. Beck, A. Kohen, Y. Dagan, and G. Deutscher. Tunneling spectroscopy: A probe for high-T_c superconductivity. *Microelectronics Journal*, 39(11):1296–1299, 2008.
- [10] A. Damascelli, Z. Hussain, and Z. X. Shen. Angle-resolved photoemission studies of the cuprate superconductors. *Reviews of Modern Physics*, 75(2):473–541, 2003.

- [11] A. Di Chiara, F. Fontana, G. Peluso, and F. Tafuri. Influence of the proximity effect on the conductance characteristics of superconducting point-contact junctions: Basic assumptions. *Physical Review B*, 48(9):6695–6698, 1993.
- [12] A. DiChiara, F. Lombardi, F. M. Granozio, U. S. diUccio, M. Valentino, F. Tafuri, A. DelVecchio, M. F. DeRiccardis, and L. Tapfer. Structure and morphology of MgO/YBa₂Cu₃O_{7-δ} bilayers for biepitaxial junctions. *Physica C*, 273(1-2):30–40, 1996.
- [13] G. Elhalel, R. Beck, G. Leibovitch, and G. Deutscher. Transition from a mixed to a pure d-wave symmetry in superconducting optimally doped YBa₂Cu₃O_{7-δ} thin films under applied fields. *Physical Review Letters*, 98(13):4, 2007.
- [14] M. Fogelstrom, D. Rainer, and J. A. Sauls. Tunneling into current-carrying surface states of high-Tc superconductors. *Physical Review Letters*, 79(2):281–284, 1997.
- [15] Y. Gao, T. J. Wagener, J. H. Weaver, B. Flandermeyer, and D. W. Capone. Reaction and intermixing at metal-superconductor interfaces- Fe/YBa₂Cu₃O_{7-δ}. *Applied Physics Letters*, 51(13):1032–1034, 1987.
- [16] D. Gustafsson. *Nanoscale YBa₂Cu₃O_{7-δ} devices -Searching for a subdominant order parameter using a single electron transistor*. Thesis, 2012.
- [17] D. Gustafsson, D. Golubev, M. Fogelstrom, T. Claeson, S. Kubatkin, T. Bauch, and F. Lombardi. Fully gapped superconductivity in a nanometresize YBa₂Cu₃O_{7-δ} island enhanced by a magnetic field. *Nature Nanotechnology*, 8(1):25–30, 2013.
- [18] b. c. . H. Kamerlingh Onnes, Commun. Phys. Lab. Univ.Leiden 120b. "further experiments with liquid helium. c. on the change of electric resistance of pure metals at very low temperatures, etc. iv. the resistance of pure mercury at helium temperatures. *Commun. Phys. Lab. Univ.Leiden*, 120b, 122b, 124b, 1911.
- [19] C. C. Homes, S. V. Dordevic, D. A. Bonn, R. Liang, W. N. Hardy, and T. Timusk. Coherence, incoherence, and scaling along the c-axis of YBa₂Cu₃O_{7-δ}. *Physical Review B*, 71(18):184515, 2005.
- [20] S. Kashiwaya, Y. Tanaka, M. Koyanagi, H. Takashima, and K. Kajimura. Origin of zero-bias conductance peaks in high-Tc superconductors. *Physical Review B*, 51(2):1350–1353, 1995.
- [21] R. Khasanov, S. Strassle, D. Di Castro, T. Masui, S. Miyasaka, S. Tajima, A. Bussmann-Holder, and H. Keller. Multiple gap symmetries for the order parameter of cuprate superconductors from penetration depth measurements. *Physical Review Letters*, 99(23):4, 2007.
- [22] J. R. Kirtley, C. C. Tsuei, A. Ariando, C. J. M. Verwijs, S. Harkema, and H. Hilgenkamp. Angle-resolved phase-sensitive determination of the in-plane gap symmetry in YBa₂Cu₃O_{7-δ}. *Nature Physics*, 2(3):190–194, 2006.

- [23] J. R. Kirtley, S. Washburn, and D. J. Scalapino. Origin of the linear tunneling conductance background. *Physical Review B*, 45(1):336–346, 1992.
- [24] K. Krishana, N. P. Ong, Q. Li, G. D. Gu, and N. Koshizuka. Plateaus observed in the field profile of thermal conductivity in the superconductor $\text{Bi}_2\text{Sr}_2\text{CaCu}_2\text{O}_8$. *Science*, 277(5322):83–85, 1997.
- [25] R. B. Laughlin. Magnetic induction of $d_{x^2-y^2}+id_{xy}$ order in high-Tc superconductors. *Physical Review Letters*, 80(23):5188–5191, 1998.
- [26] H. Maeda, Y. Tanaka, M. Fukutomi, T. Asano, K. Togano, H. Kumakura, M. Uehara, S. Ikeda, K. Ogawa, S. Horiuchi, and Y. Matsui. New high-Tc superconductors without rare earth element. *Physica C: Superconductivity*, 153–155, Part 1(0):602–607, 1988.
- [27] E. Maxwell. Isotope effect in the superconductivity of mercury. *Physical Review*, 78(4):477–477, 1950.
- [28] S. Nawaz. *Approaching the depairing critical current in superconducting $\text{YBa}_2\text{Cu}_3\text{O}_{7-\delta}$ nanowire*. Thesis, 2013.
- [29] M. R. Norman. The challenge of unconventional superconductivity. *Science*, 332(6026):196–200, 2011.
- [30] M. R. Norman, D. Pines, and C. Kallin. The pseudogap: friend or foe of high Tc? *Advances in Physics*, 54(8):715–733, 2005.
- [31] M. Oshima, Y. Yamada, T. Kawamura, S. Maeyama, K. Hohkawa, Y. Tazoh, and T. Miyahara. Surface and interfaces of high-Tc superconductors for contact and junction formation studied with synchrotron radiation photoemission spectroscopy. *Japanese Journal of Applied Physics Part 2-Letters & Express Letters*, 27(11):L2233–L2236, 1988.
- [32] W. E. Pickett. Electronic structure of the high-temperature oxide superconductors. *Reviews of Modern Physics*, 61(2):433–512, 1989.
- [33] A. Schilling, M. Cantoni, J. D. Guo, and H. R. Ott. Superconductivity above 130 k in the HgBaCaCuO system. *Nature*, 363(6424):56–58, 1993. 10.1038/363056a0.
- [34] Z. Z. Sheng and A. M. Hermann. Bulk superconductivity at 120k in the TiCaBaCuO system. *Nature*, 332(6160):138–139, 1988.
- [35] F. Steglich, J. Aarts, C. D. Bredl, W. Lieke, D. Meschede, W. Franz, and H. Schäfer. Superconductivity in the presence of strong pauli paramagnetism: CeCu_2Si_2 . *Physical Review Letters*, 43(25):1892–1896, 1979.

-
- [36] Y. Suzuki, T. Kusaka, A. Aoki, T. Aoyama, T. Yotsuya, and S. Ogawa. The contact resistance of the $\text{YBa}_2\text{Cu}_3\text{O}_{7-\delta}$ -metal film system. *Japanese Journal of Applied Physics Part 1-Regular Papers Short Notes & Review Papers*, 28(12):2463–2467, 1989.
- [37] F. Tafuri, A. Di Chiara, F. Fontana, F. Lombardi, and G. Peluso. Proximity high transmittance microjunctions in presence of a magnetic field. *Physica B: Condensed Matter*, 218(1–4):130–133, 1996.
- [38] Y. Tanaka and S. Kashiwaya. Theory of tunneling spectroscopy of d-wave superconductors. *Physical Review Letters*, 74(17):3451–3454, 1995.
- [39] M. Tinkham. *Introduction to Superconductivity*. Dover Publications, New York, 2nd edition, 2004.
- [40] C. C. Tsuei, J. R. Kirtley, C. C. Chi, L. S. Yujahnes, A. Gupta, T. Shaw, J. Z. Sun, and M. B. Ketchen. Pairing symmetry and flux-quantization in a tricrystal superconducting ring of $\text{YBa}_2\text{Cu}_3\text{O}_{7-\delta}$. *Physical Review Letters*, 73(4):593–596, 1994.
- [41] M. T. Tuominen, J. M. Hergenrother, T. S. Tighe, and M. Tinkham. experimental-evidence for parity based $2e$ periodicity in a superconducting single-electron transistor. *Physical Review Letters*, 69(13):1997–2000, 1992.
- [42] C. Weber, A. M. Klushin, S. Beuven, A. van der Hart, H. Kohlstedt, R. Semerad, and W. Prusseit. High temperature josephson bicrystal junctions and arrays for metrological applications. *Ieee Transactions on Applied Superconductivity*, 9(2):4162–4165, 1999.
- [43] M. K. Wu, J. R. Ashburn, C. J. Torng, P. H. Hor, R. L. Meng, L. Gao, Z. J. Huang, Y. Q. Wang, and C. W. Chu. Superconductivity at 93 k in a new mixed-phase y-ba-cu-o compound system at ambient pressure. *Physical Review Letters*, 58(9):908–910, 1987.
- [44] B. Wuyts, V. V. Moshchalkov, and Y. Bruynseraede. Resistivity and hall effect of metallic oxygen-deficient $\text{YBa}_2\text{Cu}_3\text{O}_{7-\delta}$ films in the normal state. *Physical Review B*, 53(14):9418–9432, 1996.
- [45] D. N. Zheng, A. M. Campbell, J. D. Johnson, J. R. Cooper, F. J. Blunt, A. Porch, and P. A. Freeman. Magnetic susceptibilities, critical fields, and critical currents of co- and zn-doped $\text{YBa}_2\text{Cu}_3\text{O}_{7-\delta}$. *Physical Review B*, 49(2):1417–1426, 1994.